https://doi.org/10.5194/acp-2020-591
Preprint. Discussion started: 29 June 2020

Atmospheric Chemistry and Physics
Discussions

Insights into the aging of biomass burning aerosol from satellite observations and 3D atmospheric modeling: Evolution of the aerosol optical properties in Siberian wildfire plumes

Igor B. Konovalov[1], Nikolai A. Golovushkin[1], Matthias Beekmann[2], and Meinrat O. Andreae[3,4,5]

[1]Institute of Applied Physics, Russian Academy of Sciences, Nizhniy Novgorod, Russia
[2]LISA/IPSL, Laboratoire Interuniversitaire des Systèmes Atmosphériques, UMR CNRS 7583, Université Paris Est Créteil (UPEC) et Université Paris Diderot (UPD), France
[3]Max Planck Institute for Chemistry, Mainz, Germany
[4]Scripps Institution of Oceanography, University of California San Diego, La Jolla, CA 92093, USA
[5]Department of Geology and Geophysics, King Saud University, Riyadh, Saudi Arabia

Correspondence to: Igor B. Konovalov (konov@ipfran.ru)

Abstract. Long-range transport of biomass burning (BB) aerosol from regions affected by wildfires is known to have a significant impact on the radiative balance and air quality in receptor regions, including the Arctic. However, the atmospheric evolution of the optical properties of BB aerosol during the long-range transport events is insufficiently understood, limiting the adequacy of representations of the aerosol processes in chemistry transport and climate models. Here we introduce a framework to infer and interpret changes of the optical properties of BB aerosol from satellite observations of multiple BB plumes. Our framework includes (1) a procedure for analysis of available satellite retrievals of the absorption and extinction aerosol optical depths (AAOD and AOD) and single scattering albedo (SSA) as a function of the BB aerosol photochemical age, and (2) a representation of the AAOD and AOD evolution with a chemistry transport model (CTM) involving a simplified volatility basis set (VBS) scheme with a few adjustable parameters. We apply this framework to analyze a large-scale outflow of BB smoke plumes from Siberia toward Europe that occurred in July 2016. We use AAOD and SSA data derived from OMI (Ozone Monitoring Instrument) satellite measurements in the near-UV range along with 550 nm AOD and carbon monoxide (CO) columns retrieved from MODIS (Moderate Resolution Imaging Spectroradiometer) and IASI (Infrared Atmospheric Sounding Interferometer) satellite observations, respectively, to infer changes in the optical properties of Siberian BB aerosol due to its atmospheric aging and to get insights into the processes underlying these changes. Using the satellite data in combination with simulated data from the CHIMERE CTM, we evaluate the enhancement ratios (EnR) that allow isolating AAOD and AOD changes due to oxidation and gas-particle partitioning processes from those due to other processes, including transport, deposition, and wet scavenging. The behavior of EnRs for AAOD and AOD is then characterized using nonlinear trend analysis. It is found that the EnR for AOD strongly increases (by about a factor of 2) during the first 20-30 hours of the analyzed evolution period, whereas the EnR for AAOD does not exhibit a statistically significant increase during this period. The increase in AOD is accompanied by a statistically significant enhancement of SSA. Further BB aerosol aging (up to several days) is associated with a strong decrease of EnRs for both AAOD and AOD. Our simulations constrained by the observations indicate that the upward trends in EnR for AOD and in SSA are mainly due to atmospheric processing of secondary organic aerosol (SOA), leading to an increase in the mass scattering efficiency of BB aerosol. Evaporation and chemical fragmentation of the SOA species, part of which is assumed to be absorptive (to contain brown carbon), are identified as a likely reason for the subsequent decrease of the EnR for both AAOD and AOD. Hence, our analysis reveals that the long-range transport of smoke plumes from Siberian fires is associated with major changes in BB aerosol optical properties and chemical composition. Overall, this study demonstrates the feasibility of using available satellite observations for evaluating and improving representations in atmospheric models of the BB aerosol aging processes in different regions of the world at much larger temporal scales than those typically addressed in aerosol chamber experiments.

1 Introduction

Open biomass burning – including wildfires, controlled fires, and agricultural burns – is an important source of aerosol particles that are a key agent in the processes controlling regional and global climate (e.g., Bond et al., 2013; Jacobson, 2014; Sand et al., 2015). Climate effects of biomass burning (BB) aerosol are associated, in particular, with the scattering of the solar radiation by organic matter, which is typically a dominant component of BB aerosol (Reid et al., 2015a), as well as with absorption of solar radiation by black carbon (BC) and brown carbon (BrC), which are also ubiquitous components of BB aerosol (Andreae and Gelencsér, 2006), both within the atmosphere and on snow and ice surfaces (Gustafson and Ramanathan, 2016; Jiang et al., 2016; Wang et al., 2016). Acting as cloud condensation nuclei (CCN), BB aerosol particles can affect the formation and radiative characteristics of clouds (e.g., Hobbs et al., 1969; Petters et al., 2009; Lu et al., 2018). Apart from being an important agent in the climate system, BB aerosol is a major contributor to air pollution episodes that have been caused by wildfires worldwide (e.g., Konovalov et al., 2011; Keywood et al., 2013; Gupta et al., 2018) and represent a major human health problem (Lelieveld et al., 2020). These facts highlight the importance of having adequate representations of the physical and chemical properties of BB aerosol in models of various complexities for climate and air pollution studies. However, developing such representations is an extremely challenging task, given the high diversity of BB aerosol composition and optical properties (e.g., Reid et al., 2005a,b; Tsigaridis and Kanakidou, 2018), and the dynamic, nonlinear nature of the atmospheric evolution of its organic component (e.g., Bian et al., 2017; Konovalov et al., 2019).

The composition of primary BB smoke is strongly dependent on fuel type and highly variable burning conditions (McMeeking et al., 2009; Levin et al., 2010; Liu et al., 2014; Laskin et al., 2015). For example, smoldering fires have been reported to favor higher emissions of organic aerosol (OA) and semi-volatile organic gases, but lower BC emissions, compared to flaming conditions (Jen et al., 2019). In turn, the BC-to-OA ratio has been identified as a key factor controlling BrC contribution to light absorption by BB aerosol (Saleh et al., 2014; Lu et al., 2015; Pokhrel et al., 2017; McClure et al., 2020).

Furthermore, results of laboratory and field studies show a very diverse picture of atmospheric transformations of BB aerosol, suggesting that oxidation of volatile and semi-volatile organic gases or heterogeneous oxidation of particles can lead, in different cases, to either enhancements or losses of organic matter by BB aerosol (e.g., Yokelson et al. 2009; Cubison et al., 2011; Hennigan et al., 2011; Akagi et al., 2012; Jolleys et al., 2015; Konovalov et al., 2015; Tiitta et al., 2016; Ciarelli et al., 2017; Vakkari et al., 2018). Besides, some observational studies reported that atmospheric aging of BB aerosol did not result in changes of mass concentration (corrected for dilution) of OA (e.g., May et al.; 2015; Sakamoto et al. 2015; Zhou et al., 2017). This diversity, which is presently not well understood and is not reproduced in chemistry transport and climate models, can, at least partly, be associated with differences in fuel types, burning conditions, initial parameters of BB smoke plumes, and the dilution rate (Hennigan et al., 2011; Ahern et al., 2019; Lim et al., 2019; Hodshire et al. 2019; Konovalov et al., 2019).

There is still no consensus on the patterns of the changes of absorptive properties associated with brownness of organics in BB aerosol in the real atmosphere, although findings from many laboratory and field studies indicate that these changes can be very significant (e.g., Kumar et al., 2018; Browne et al., 2019; Fan et al., 2019; Li et al., 2019; Sumlin et al., 2019). Based on both a BB aging experiment with an outdoor smog chamber and an analysis of field observations, Zhong and Jang (2014) reported an initial increase in light absorption by BrC under natural sunlight, followed by a decrease. The same BrC aging effects, that is, an initial photo-enhancement of BrC absorption and an eventual bleaching of OA under the UV irradiation, have also been found in more recent laboratory experiments with water-soluble organic extracts from BB aerosol (Wong et al., 2017; 2019). However, only rapid bleaching of BrC (on the time scale of 9 to 15 hours) has been detected in age-resolved aircraft observations of BB aerosol (Forrister et al., 2015). Furthermore, while these aircraft observations suggest that BrC almost fully disappears from BB aerosol after about 40 hours of atmospheric aging, an analysis of the AErosol RObotic NETwork (AERONET) data by Wang et al. (2016) indicates that a sizeable fraction of BrC "survives" during a much longer atmospheric exposition. Laboratory data (Di Lorenzo et al., 2017; Wong et al., 2017; 2019; Fleming et al., 2020) indicate that this recalcitrant fraction is likely formed by high-molecular-weight chromophores (while low-molecular-weight chromophores are more rapidly destroyed), suggesting that the atmospheric fate of the BrC fraction of BB aerosol is dependent on fuel type and burning conditions. Finally, it should be noted that the atmospheric relevance of various processes, which, according to laboratory studies, can affect formation and bleaching of chromophores in BB aerosol, is so far not sufficiently clear (Fleming et al., 2020); this fact constitutes an additional obstacle for developing adequate modeling representations of BB aerosol aging processes.

The discussion above indicates that the sparse and often contradictory results of field and laboratory studies available so far can hardly provide consistent observational constraints for representations of the effects of atmospheric aging of BB aerosol in chemistry-transport and climate models. The general objective of the present study is to find a way to infer statistically reliable information on the impact of aging processes on the optical properties of BB aerosol from available satellite measurements. To this end, we developed an analytical framework enabling the synergetic combination of satellite and model data on the BB aerosol optical properties and composition. Unlike the inevitably sparse field observations that are available only for a tiny fraction of wildfires occurring in the world each year, satellite instruments provide abundant observations of BB plumes associated with virtually any major vegetation fire worldwide. Accordingly, satellite observations of BB plumes can enable statistical characterization of the BB aerosol aging effect in a given region, encompassing a wide range of BB aerosol sources and burning conditions. A similar concept was initially exploited in our previous study (Konovalov et al., 2017a), focusing on the analysis of the MODIS (Moderate Resolution Imaging Spectroradiometer) observations of extinction aerosol optical depth (AOD) (Levy et al., 2013) in Siberia. We found, in particular, that after being corrected for dilution, AOD increases almost two-fold in BB plumes aged between 15 and 20 hours, compared to fresher plumes, indicating strong secondary organic aerosol (SOA) formation. This study substantially extends the scope of the previous one by analyzing satellite observations of both absorption and extinction characteristics of BB aerosol. Specifically, along with the MODIS AOD observations, we analyze near-UV retrievals of the absorption aerosol optical depth (AAOD) and single scattering albedo (SSA) from the OMI (Ozone Monitoring Instrument) measurements (Torres et al., 2007; 2013). Taking into account that the OMI observations of AAOD at the 388 nm wavelength are sensitive to the BrC content in the BB aerosol (Jethva et al., 2011; Mok et al., 2016), these observations can be expected to provide useful insights into the changes of the absorptive properties of the organic fraction of BB aerosol. At the same time, the MODIS AOD observations are expected to bring light to a possible role of SOA formation (Saleh et al., 2013) in these changes. Note that the OMI AAOD and MODIS AOD observations were earlier found to provide consistent information on BB aerosol optical properties, enabling their use as observational constraints on BB emissions of BC and OC (Konovalov et al., 2018). The OMI AAOD retrievals were also found to provide useful constraints on anthropogenic BC emissions over southeastern Asia (Zhang et al., 2015). Similar to Konovalov et al. (2017a), we additionally use CO column amounts retrieved from IASI (Infrared Atmospheric Sounding Interferometer) satellite observations (Clerbaux et al., 2009) to account for the effects of dilution.

To analyze and interpret the satellite observations, we use the CHIMERE chemistry transport model (Mailler et al., 2017) in combination with an external module, OPTSIM (Stromatas et al., 2012), enabling Mie calculations of the light absorption and extinction for both core-shell and homogeneous morphologies of particles. The CHIMERE simulations are also used to estimate the photochemical age of BB aerosol. A mechanistic (highly simplified) representation of evolution of the organic fraction of BB aerosol within the VBS framework (Robinson et al., 2007) is used to simulate the behavior of mass concentrations of primary and secondary organic components of BB aerosol. It should be noted that there is currently no uniform way to represent atmospheric transformations of BB OA and its optical properties in models. Furthermore, differences between the available VBS schemes (e.g., Shrivastava et al., 2015; Konovalov et al., 2015; Ciarelli et al., 2017; Tsimpidi et al., 2018), which have been proposed for simulations of BB aerosol and are, to some extent, constrained by observational or experimental data, have been shown to result in major quantitative and qualitative differences in the simulated multi-day evolution of BB OA mass concentration (Konovalov et al., 2019). There is also no uniform way to represent sources and evolution of BrC. Typically, BrC has been introduced in previous modeling studies as an absorbing fraction of otherwise non-absorbing OA (e.g., Park et al., 2010; Saleh et al., 2015; Jo et al., 2016), with pre-defined absorptive properties that are not affected by atmospheric aging. More recently, Wang et al. (2018), Brown et al. (2018), and Zhang et al. (2020) assigned empirical estimates of absorption properties for all OA in their global modeling studies, and also assumed that the absorption of OA is decreasing with a constant rate as a function of the BB aerosol photochemical age, irrespective of the simulated evolution of the chemical composition of the particles. In this study, we largely follow the latter approach but take a step forward by considering evolution of BrC consistently with simulated changes of both primary organic aerosol (POA) and SOA. Several parameters of our model are adjusted to meet the observational constraints. Nonetheless, because our representation of BB aerosol aging is highly simplified and associated with large uncertainties, we use our simulations mainly to get insights into qualitative patterns of the BB aerosol transformations, rather than for quantitative characterization of any processes.

Aerosol particles emitted from vegetation fires in Siberia can be transported in the atmosphere over thousands of kilometers and significantly affect atmospheric composition in receptor regions, such as, e.g., East Asia (Agarwal et al., 2010; Matsui et al, 2013, Ikeda et al., 2015; Yasunari et al., 2018), the Western USA (Laing et al., 2016), and Alaska (Warneke et al., 2009). Siberian fires have been estimated to contribute, on average, up to 40 % of total BC deposited annually in the Arctic (Evangelio et al., 2016), where BB aerosol can significantly affect the climate processes (Sand et al., 2015) associated with an observed rapid increase of the annual surface temperature in this region (Bekryaev et al., 2010). As the role of fires in boreal regions is projected to increase in a warmer climate (Oris et al., 2014), there is a need for better quantitative understanding of the climate impact of BB aerosol – specifically from Siberian fires –, which can be achieved, in particular, through the use of stronger observational constraints to represent of BB aerosol optical properties and their evolution in chemistry transport and climate models. A way to obtain and exploit such constraints is proposed in this paper.

In this study, we analyze aging effects on the evolution of BB aerosol from Siberian fires by considering a relatively short period – from 15 to 31 July 2016. This analysis period is chosen to include a spectacular event of an anomalous outflow of optically dense BB plumes from Siberia to the European part of Russia. Different aspects of this event have already been addressed in the scientific literature (e.g., Sitnov et al., 2017; 2020; Gorchakov et al., 2017). It has been shown, in particular, that this event was associated with the formation of a so-called dipole structure of the atmospheric circulation, with the westward transport of air masses being a result of anticyclonic (clockwise) and cyclonic (counterclockwise) circulations to the north and the south of the air transport trajectory, respectively. The outflow of the BB plumes took place in a relatively dry, predominantly cloudless atmosphere, providing nearly ideal conditions for observing the evolution of BB smoke plumes from space. Importantly, the geographical isolation of aged and young plumes during this event allows us to minimize the effects of possible uncertainties associated with the estimation of photochemical age.

To the best of our knowledge, this is the first study attempting to constrain simulations of the aging behavior of BB aerosol with satellite observations of both absorption and extinction AODs. Using the constrained simulations, we attempt to get insights into the key physical and chemical processes driving changes of the optical characteristics of BB aerosol from Siberian wildfires during its long-range transport. Although this study addresses only a relatively short period and a specific region, we believe that the analytical framework developed here, as well as insights into the effects of atmospheric aging of BB aerosol during a period spanning its typical lifetime, will be beneficial for other studies involving modeling of aerosol processes and their climate impacts, especially in Northern Eurasia and in the Arctic.

https://doi.org/10.5194/acp-2020-591
Preprint. Discussion started: 29 June 2020

2 Method and data

2.1 Analysis method

We analyze the atmospheric evolution of BB aerosol by considering the enhancement ratio (EnR), which is defined as the ratio of the enhancement of actual AAOD or AOD due to fire emissions to the corresponding enhancement of an inert aerosol tracer that is assumed to be composed of non-volatile matter. In accordance to this definition, the enhancement ratio for AAOD (EnR_{abs}) is evaluated as follows:

$$EnR_{abs} = \eta_0 \frac{\tau_{abs} - \tau_{abs}^{bgr}}{\tau_{abs}^{t}}, \tag{1}$$

where τ_{abs} is the AAOD retrieval, τ_{abs}^{bgr} is the estimate of the background part of AAOD, τ_{abs}^{t} is the estimate of AAOD associated with the inert aerosol tracer, and η_0 is a constant normalization factor defined below. The enhancement ratio for extinction AOD (EnR_{ext}) is evaluated similar to EnR_{abs}, by substituting the observed and estimated AOD values (τ_{ext}, τ_{ext}^{bgr}, and τ_{ext}^{t}) into Eq. (1) instead of τ_{abs}, τ_{abs}^{bgr}, and τ_{abs}^{t}. The idea behind the use of these EnRs in our study is to isolate changes of AAOD and AOD due to oxidation and condensation/evaporation processes from those due to any other processes, such as, e.g., advection, eddy diffusion, dry deposition, and wet scavenging, which can affect AAOD and AOD associated with BB plumes. In other words, the analysis of EnRs is expected to reveal the differences between the dynamics of AAOD or AOD in the real BB plumes and in a hypothetical simulation in which BB aerosol is assumed to consist of only non-volatile material and SOA formation processes are disregarded. In our analysis involving EnRs, we largely follow Konovalov et al. (2017a) and Konovalov et al. (2019), but it should also be noted that the meaning of EnR defined by Eq. (1) is very similar to that of the normalized excess mixing ratio (NEMR), which was employed in previous studies (e.g., Yokelson et al., 2009; Vakkari et al., 2018; Junghenn Noyes et al., 2020) to analyze the evolution of mass concentrations (or mixing ratios) of aerosol species. In the framework of this study, Eq. (1) is also used to analyze the simulated evolution of BB aerosol. To this end, AAOD (or AOD) retrievals are replaced in Eq. (1) by the corresponding simulated values.

As the main option for our analysis, the BB aerosol tracers (τ_{abs}^{t} and τ_{ext}^{t}) are evaluated using AAOD and AOD values obtained from simulations with a chemistry transport model (CTM) as explained in Sect. 2.3. An advantage of the BB aerosol "optical" tracers in comparison with more traditional tracers based on CO concentration is that they are affected not only by transport and eddy diffusion but also by dry deposition, wet scavenging, and coagulation, thereby representing BB aerosol in the aforementioned hypothetical simulation. Note that coagulation is not considered as one of the BB aerosol aging processes addressed in this study.

However, the BB aerosol simulated tracers can be affected by model transport errors that can lead to biases in EnRs for both fresh and aged BB plumes observed from satellites (Konovalov et al., 2017a). To address this potential issue, we employ a simple correction procedure involving satellite observations of CO columns. Specifically, we introduce a correction factor, f_c, defined as follows:

$$f_c = ([CO]^{obs} - [CO]^{bgr})\,([CO]^{mod})^{-1}, \tag{2}$$

where $[CO]^{obs}$ and $[CO]^{mod}$ are the observed total CO column amounts and the corresponding modeled contribution of fire emissions to the CO columns, respectively, and $[CO]^{bgr}$ is the background value of [CO] in the absence of fires.

This factor is applied to the simulated tracers. In particular, the simulated values of τ_{abs}^{t} are corrected as follows:

$$\tau_{abs}^{t}[corrected] = \tau_{abs}^{t}[simulated] \times f_c \tag{3}$$

This correction implies that the simulated CO column amounts in a BB plume are affected by the same multiplicative transport errors as the BB aerosol components determining AAOD and AOD. Note that a similar procedure was used in Konovalov et al. (2017a), where advantages of using the observed and simulated CO columns in the estimation of EnR for AOD are discussed in detail; similar arguments apply for our estimations of EnRs for AAOD and AOD in this study. Estimation of the background values of τ_{abs}, τ_{ext}, and [CO] in this study is described in Sect. 2.3.

The normalization factor η_0 does not affect the results of our analysis and is introduced mainly for illustrative purposes. Here, we define it such that the average of all values of EnR_{abs} (or EnR_{ext}) over the ensemble of the data considered is equal to one:

$$\eta_0 = \left\langle \frac{\tau_{abs} - \tau_{abs}^{bgr}}{\tau_{abs}^{t}} \right\rangle^{-1}, \tag{4}$$

where the angular brackets denote averaging over the data ensemble.

As part of our analysis, we infer trends of EnRs for AAOD and AOD in the process of BB aerosol aging from the ensemble of available estimates of EnR_{abs} and EnR_{ext}. To characterize the BB aerosol age, we evaluate the time, t_e, of exposure of a given BB plume to solar irradiation. In other words, t_e is the integral time of the transport of a given BB plume since emission, during daytime hours. This characteristic is evaluated as detailed in Sect. 2.3. For brevity, we refer below to t_e as the photochemical age of BB aerosol. Note that t_e is equivalent to the more conventional definition of the BB aerosol photochemical age (e.g., Konovalov et al., 2017a) in the case where the latter is evaluated with constant daytime and zero nighttime OH concentrations within the BB plume. Unlike the BB aerosol photochemical age evaluated in Konovalov et al. (2017a), the solar irradiation exposure time – which was previously employed by Forrister et al. (2015) to evaluate the photo-degradation of BrC in observed BB plumes – is not affected by potential major uncertainties in the simulated OH concentration. A potential drawback of using the solar irradiation exposure time as a predictor for the atmospheric evolution of BB aerosol in an analysis such as ours is that it can result in losing some observational information about the oxidation processes controlled by OH.

The trends in EnR_{abs} and EnR_{ext} (that is, the corresponding dependences on t_e) are fitted with a nonlinear function, $y(t_e)$, which is constructed as a sum of sigmoids:

$$y(t_e) = \sum_{k=1}^{N} \frac{w_{k1}}{(1+\exp(w_{k2}t_e + w_{k3}))} + w_0, \tag{5}$$

https://doi.org/10.5194/acp-2020-591
Preprint. Discussion started: 29 June 2020

where w_{1k}, w_{2k}, w_{3k}, and w_0 are the weight coefficients, and N is the number of sigmoids. In essence, the function $y(t_e)$ represents a neural network (of the perceptron type), which is known as a universal approximator (Hornik et al., 1989). The optimal values of the weight coefficients are found by minimizing the root mean square difference between the individual values of $\mathrm{EnR_{abs}}$ or $\mathrm{EnR_{ext}}$ and the corresponding values of y (t_e). Following Konovalov et al. (2010), the optimization of the weight coefficients is achieved using the Nelder-Mead simplex algorithm (Press et al., 1992). Although the number of neurons (N) used for the trend approximation can also be optimized in a regular (albeit more complicated) way (Konovalov et al., 2010), here we simply tried the fits with $N=1$, $N=2$, and $N=3$. We found that while the fits with $N=2$ manifested statistically significant features that are missing in the approximations with $N=1$, the use of three neurons instead of two did not reveal any new statistically significant features of the analyzed trends. Therefore, only results obtained only with $N=2$ are reported in this paper. The nonlinear fit function given by Eq. (5) is also applied to the SSA retrievals described in Sect. 2.2 as well as to model data described in Sect. 2.3. Similar to Konovalov et al. (2017a), the confidence intervals for the approximations $y(t_e)$ were evaluated with the bootstrapping method (Efron and Tibshirani, 1993) involving a random selection of sample estimates. To ensure the reliable evaluation of the confidence intervals in terms of the 95th percentile, the analysis involved 300 random samples. Some technical differences between the analysis procedures used in Konovalov et al. (2017a) and this study are discussed in Supplementary Material, Sect. S1.

2.2 Satellite data

Our analysis described in the previous section makes use of aerosol optical properties and total CO column amounts, which are retrieved from satellite observations performed by the three satellite instruments: OMI (Levelt et al., 2006), MODIS (Salomonson et al., 1989), and IASI (Clerbaux et al., 2009). Various combinations of these satellite retrievals were used in our previous studies of the atmospheric impacts of Siberian fires (Konovalov et al., 2014; 2017a; 2018) and are only briefly described below. Pre-processing and harmonization of the different satellite data sets are explained in Sect. 2.5.

Specifically, we used the AAOD and SSA retrievals for the 388 nm wavelength, which are available as part of the Level-2 OMAERUV (v. 1.8.9.1) data product (Torres et al., 2007, 2013) derived by NASA from the OMI observations onboard the EOS Aura satellite. The OMAERUV algorithm exploits the observed departure of the spectral dependence of the near-UV upwelling radiation at the top of the atmosphere from that of a hypothetical pure molecular atmosphere and derives AAOD, AOD, and SSA following a look-up table approach with assumed aerosol models, aerosol layer height and surface albedo. Importantly, the OMAERUV data product used in this study accounts for the wavelength-dependent aerosol absorption associated with BrC (Jethva et al. 2011; Torres et al., 2013). While the OMAERUV algorithm identifies one of the three assumed aerosol types (biomass burning, desert dust, and urban/industrial), we consider the AAOD and SSA data only for the first aerosol type. The data are retrieved assuming a set of five different vertical locations of the aerosol center mass: at the surface and 1.5, 3.0, 6.0, and 10 km above the surface. We also used the “final” AAOD OMAERUV product, which is derived using the OMI-CALIOP (Cloud-Aerosol Lidar with Orthogonal Polarization) joint dataset (Torres et al., 2013) for the monthly climatology of the aerosol layer height. An important feature of the OMAERUV data product is that the AAOD data are less affected by sub-pixel cloud contamination than the AOD and SSA data, due to partial cancellation of errors in the AOD and SSA retrievals. Accordingly, the quality assured AOD and SSA data (which are associated with the quality flag "0") are much less abundant than the quality assured AAOD data (which are associated with the quality flag "0" and "1"). Both AOD and SSA data were found to be in a rather good agreement with corresponding AERONET data worldwide (Ahn et al., 2014; Jethva et al., 2014), indicating that the AAOD data associated with the quality flag "0" are also sufficiently accurate. Besides, in our previous study (Konovalov et al., 2018), CTM simulations based on BB BC emissions in Siberia, which were inferred from the OMI AAOD data associated with the quality flag of both 0 and 1, were found to be consistent with AERONET, aircraft, and in-situ aerosol measurements. Furthermore, the relationship between AAOD and AOD values retrieved from, respectively, the OMI and MODIS satellite observations was found to be virtually the same as that between AAOD and AOD values derived from the AERONET measurements in Siberia, confirming that sub-pixel cloud contamination, which can affect the less reliable retrievals (with the quality flag "1"), is not likely to result in serious biases in the OMI AAOD retrievals. Therefore, the previous results provide evidence for the reliability of the OMAERUV AAOD data corresponding to both values of the quality flag.

We also used AOD at 550 nm derived from the MODIS observations onboard the Aqua and Terra satellites (Levy et al., 2013). The AOD data are obtained as the merged "dark target" and "deep blue" AOD retrievals from the Collection 6.1 MYD04 and MOD04 Level-2 data products (Levy et al., 2015). Validation studies (e.g., Levy et al., 2010) indicated the high quality of the MODIS AOD data, with the multiplicative and additive errors of MODIS-retrieved AOD of ~15% and 0.05 (or less), respectively.

In this study, the OMI AAOD and MODIS AOD retrievals are analyzed independently as described in Sect. 2.1. Besides, a similar analysis was performed for the SSA estimates obtained by combining the AAOD and AOD data as follows:

$$\omega_0 = \frac{\tau_{ext}^{inferred} - \tau_{abs})}{\tau_{ext}^{inferred}}, \qquad (6)$$

where ω_0 is an estimate of SSA at 388 nm, τ_{abs} is AAOD retrieved from the OMI measurements, and $\tau_{ext}^{inferred}$ is AOD at 388 nm inferred from the MODIS observations at 550 nm using a power-law approximation. The extinction Ångström exponent necessary for this calculation was estimated in two ways. First, it was evaluated as the average ratio of the logarithms of the 388-nm AOD and 550-nm AOD retrievals from the matching OMI and MODIS satellite observations, respectively. Since the OMI AOD data correspond to the quality flag "0" and are therefore very sparse, the Ångström exponent could be estimated only as a constant number being independent on the BB aerosol age. The different AOD retrievals were matched in space and time as described below in Sect. 2.5. Second, the Ångström exponent was calculated using the simulated AOD values (see Sect. 2.3) matching both the AAOD and AOD observations. The advantage of the second approach is that it allowed us to take into account the dependence of the Ångström exponent on the BB aerosol photochemical age, but an obvious drawback of the model estimates is that they can be affected by various model errors.

The total CO columns used in our analysis were retrieved using the FORLI (Fast Optimal Retrievals on Layers for IASI) algorithm (Hurtmans et al., 2012) from the IASI observations onboard the METOP-A satellite (Clerbaux et al., 2009) and are provided by LATMOS/CNRS and ULB (ESPRI, 2020). Following Konovalov et al. (2014; 2016; 2017a), the IASI CO data were pre-selected based on the degree of freedom of the signal (DOFS), which is considered as an indicator of the IASI sensitivity to CO in the boundary layer (George et al., 2009): we only considered the CO observations with DOFS exceeding 1.7.

In addition to the satellite observations of aerosol and CO, we use MODIS retrievals of the fire radiative power (FRP), which are available as the Collection 6 Level-2 MYD14/MOD14 data products (Giglio and Justice, 2015a, b). Following Konovalov et al. (2018), these FRP data were used to evaluate fire emissions, as briefly explained in the next section.

2.3 Chemistry transport model simulations: basic configuration and fire emissions

The chemistry transport model (CTM) is a key component of our analytical framework, serving three main objectives. First, we use the model to evaluate the BB aerosol tracers and photochemical age. Second, it is used to characterize the background conditions for aerosol and CO. Third, simulations of BB aerosol evolution help interpreting the results of the satellite data analysis.

The simulations are performed with the CHIMERE CTM, version 2017 (Mailler et al., 2017). The same version of this model was successfully used in our previous analysis of satellite observations of BB aerosol (Konovalov et al., 2018). Previous versions of the CHIMERE model proved to be useful in other numerous studies of BB aerosol and fire emissions (e.g., Hodzic et al., 2010; Konovalov et al., 2012; Péré et al., 2014; Majdi et al., 2019). In this study, the configuration of the model was almost the same as that in Konovalov et al. (2018), although there are some differences mainly concerning the representations of the organic fraction and optical properties of BB aerosol. These model representations are described in Sect. 2.4. The basic features of the model configuration used in this study are outlined later in this section.

Specifically, the chemical transformations of gaseous species, including OH, are simulated with the MELCHIOR2 chemical mechanism. Photolysis rates are computed with the FAST-JX module, taking into account the attenuation of solar radiation by both clouds and aerosols. The representation of dry deposition follows Zhang et al. (2001). Wet scavenging and coagulation of aerosol particles are simulated using the standard parameterizations described in Mailler et al. (2017) and Menut et al. (2013). The formation of SOA from biogenic emissions of isoprene and terpenes is simulated with an oxidation scheme based on Kroll et al. (2006) and Zhang et al. (2007). Anthropogenic SOA is represented as a result of the oxidation of a few specific volatile SOA precursors (Bessagnet et al., 2008). The anthropogenic emissions of gaseous and aerosol species are specified using the Hemispheric Transport of Air Pollution (HTAP) v2 global emission inventory (Janssens-Maenhout et al., 2015). Biogenic emissions of several organic gases and NO are calculated using the Model of Emissions of Gases and Aerosols from Nature (MEGAN v2.04) (Guenther et al., 2006).

https://doi.org/10.5194/acp-2020-591
Preprint. Discussion started: 29 June 2020

Fire emissions are derived from satellite FRP data following the methodology detailed in Konovalov et al. (2014; 2017a; 2018). Briefly, the rate of emissions of a given aerosol or gaseous species from fires per a unit area is assumed to be proportional to the FRP density. The proportionality coefficients include, in particular, the emission factor (depending on a vegetation land cover type), the empirical factor relating FRP to the BB rate, and the adjustable correction factor (F_s), which is allowed to take different values for different species *s*. The emission factors for gaseous species are specified using the data from Andreae (2019). However, to simplify the auxiliary – for the given study – task of optimizing BB aerosol emissions, the BC and organic carbon (OC) emission factors are taken to be the same as in Konovalov et al. (2018; see Table 1 therein). The emission rates are modulated with the diurnal profile of BB emissions, which was derived directly from the MODIS FRP data (Konovalov et al., 2014, 2015). The correction factors are adjusted against the satellite data as explained in Sect. 2.6. The emission injection heights are calculated using the parameterization by Sofiev et al. (2012).

To estimate the BB aerosol photochemical age (as defined in the previous section), the chemical mechanism in CHIMERE is extended to include two gaseous tracers that have the same emissions as BB OC. One of the tracers, T_1, is treated as an inert gas, while another tracer, T_2, decays with time, but only when the local solar zenith angle is less than 90°. The decay rate, k_T, is set to be equal to $2.3\cdot10^{-5}$ s^{-1} to represent – for definiteness – the mid-range of the half-lives for the decay of BrC in BB aerosol (12 h) according to the observational estimates by Forrister et al. (2015). Using the columnar mass concentrations of the tracers, $[T_1]$, and $[T_2]$, the BB aerosol photochemical age (or, more strictly speaking, the solar radiation exposure time), t_e, is estimated as follows:

$$t_e = k_T^{-1} \ln([T_1]\,[T_2]^{-1}). \tag{7}$$

The simulations are performed using a 1 by 1 degree model mesh covering a major part of Northern Eurasia (22.5–136.5 ° E; 38.5–75.5 ° N) with 12 non-equidistant model layers in the vertical. The top of the upper layer is fixed at the 200 hPa pressure level. The model was run for the period from 28 May to 15 August 2016, but the first 18 days (until 15 June) are withheld as the spin-up period. Note that BB aerosol evolution in 2016 had not been addressed in our previous studies mentioned above. The CHIMERE simulations are driven with the meteorological data from the WRF (Weather Research and Forecasting; version 3.9) model (Skamarock et al., 2008) simulations with nudging toward the FNL reanalysis (NCEP, 2017).

Similar to Konovalov et al. (2015; 2017a), the simulations considered in this study are performed for three main scenarios. The first and second scenarios (labeled here as 'bb_vbs' and 'bb_trc', respectively) represent the conditions with predominating air pollution from fire emission. For these scenarios, all sources of gases and aerosol, except for those due to fire emissions inside the CHIMERE domain, were disregarded. The 'bb_vbs' scenario corresponds to the BB OA representation formulated within the VBS framework as described in Sect. 2.4. In the 'bb_trc' scenario, which is ancillary in the framework of the given study, the BB OA representation largely follows that for anthropogenic OA in the "standard" version of CHIMERE (Menut et al., 2003), presuming, in particular, that primary OA consists of non-volatile material. In this study, this representation is further simplified by entirely neglecting SOA formation, which turned out to be rather negligible anyway in our previous BB aerosol simulations with the standard version of CHIMERE (Konovalov et al., 2015; 2017a; 2018). The simulations for the 'bb_trc' scenario are used to evaluate the BB aerosol tracers involved in Eq. (1). For both scenarios, particulate fire emissions of OC were distributed following a fine-mode log-normal distribution with a mass median diameter (MMD) of 0.3 μm and a geometric standard deviation of 1.6 (Reid et al., 2005a) among 10 size sections. A smaller value of MMD of 0.25 μm was assumed for BC emissions, partly based on the recent measurements by Morgan et al. (2020). Taking into account that a contribution of the coarse mode of aerosol particles to the optical properties of BB aerosol at the UV and visual wavelengths is likely negligible (Reid et al., 2005b), this mode was disregarded in our simulations. This simplification allows us to avoid large uncertainties associated with the representation of emissions and the evolution of coarse particles.

The third scenario (labeled below as 'bgr') represents the hypothetical conditions that are background with respect to the air pollution caused by fire emissions. The corresponding simulations were made with anthropogenic and biogenic emissions of particles and gases, but without fire emissions. Monthly climatology for gas and aerosol concentrations from the LMDZ-INCA chemistry transport model was used as the boundary conditions. The AOD values in our analysis were computed in CHIMERE under the assumption that particle components are homogeneously mixed. The AAOD background values have not been evaluated in this study. As discussed in Konovalov et al. (2018), the main reason is that it is not known how the background part can be accounted for in the OMI AAOD retrievals for the "biomass burning" type of aerosol. Furthermore, the CHIMERE simulations of AAOD at 388 nm for the scenes dominated by anthropogenic pollution are probably highly uncertain particularly due to poorly known and variable values of the imaginary refractive index for OA. Hence, a contribution of the background part of AAOD to the OMI AAOD retrievals is effectively neglected and is disregarded (unless indicated otherwise) in the analysis involving Eq. (1). To evaluate the total CO columns and AOD representative of all sources (anthropogenic, biogenic, and pyrogenic) of gases and aerosol, the corresponding values for the 'bb_vbs' or 'bb_trc' scenarios are summed up with values for the 'bgr' scenario. Note that doing so we disregard any effects of anthropogenic emissions on the evolution of BB aerosol: according to our simulations, concentrations of aerosol and reactive gases in the analyzed situation are predominantly determined by fire emissions. Our computations of the optical properties of BB aerosol are explained in the next section.

Figure 1 shows the model domain and illustrates the fire emissions used in our simulations by presenting the density of the total BB emissions of particulate matter (PM) according to the 'bb_vbs' scenario in the analysis period of 15-31 July 2016 (see Introduction). The same figure also introduces the study region that covers western and central parts of Siberia – where (as evident from the figure) major fires occurred during the analysis period – and also a part of Eastern Europe, including the European territory of Russia and territories of several Eastern European countries.

2.4 Model representation of the evolution and optical properties of BB aerosol

As noted above, one of the goals of our BB aerosol simulations is to interpret the evolution of BB aerosol optical properties that can be inferred from satellite observations as described in the previous section. Taking into account that the real BB aerosol evolution depends on numerous variable factors, most of which cannot presently be constrained by available observations in Siberia, we do not attempt to represent the many inter-related aging processes that can affect the BB aerosol evolution in a quantitatively accurate way. Furthermore, it is also challenging to choose an appropriate model representation of BB aerosol atmospheric aging among those suggested in the literature. Typically, such representations involve organic aerosol (OA) oxidation schemes that are designed using the volatility basis set (VBS) framework (Donahue et al., 2006; Robinson et al., 2007). However, using the different VBS oxidation schemes partly constrained by laboratory measurements or atmospheric observations to simulate the multi-day BB aerosol evolution under fixed ambient conditions has been found to result in major quantitative and even qualitative differences between the simulations (Konovalov et al., 2019). Furthermore, it is not given that any of the available schemes can adequately describe the BB aerosol evolution specifically in Siberia. Hence, instead of choosing any concrete OA oxidation scheme among those previously described in the literature, we designed a highly simplified (mechanistic) VBS scheme, which can be fitted to the satellite observations by adjusting only a few parameters. This scheme was used in our simulations for the ‘bb_vbs’ scenario.

As the basis for our OA oxidation scheme, we used a relatively simple “1.5-dimensional” VBS scheme proposed and described in detail by Ciarelli et al. (2017) (abbreviated below as C17). The original scheme addresses the evolution of several surrogate organic species, each of which is given a volatility, molecular weight, and the oxidation state. More specifically, all semi-volatile organic compounds (SVOCs) are split into three sets, such as (1) the POA set, (2) the set of SOA species formed as a result of oxidation of the POA species, and (3) the SOA set containing products of oxidation of volatile organic compounds (VOCs) or intermediate-volatile organic compounds (IVOCs). Real VOC and IVOC species are represented by surrogate species referred to as NTVOCs (“non-traditional” VOCs). Some parameters of the C17 scheme, including the mass ratio of NTVOC and SVOC emissions and the enthalpies of vaporizations for SVOCs, were constrained with mass-spectrometric measurements of organic gases and particles from combustion of beech logs in a residential wood burner. The SVOC species are split into five volatility classes, with the volatilities (C^*) ranging from 10^{-1} to 10^3 μg m^{-3}. The constrained VBS scheme yielded a good agreement of the measurements with corresponding box-model simulations under OH exposures that are equivalent to about 10 to 15 hours of evolution under typical atmospheric conditions (Ciarelli et al., 2017).

Our simplified oxidation scheme includes only two aggregated volatility classes of the POA species, one of which aggregates the three original classes of organic compounds with relatively low volatilities (LV) ($C^* \in [10^{-1}; 1]$ μg m^{-3}), and another represents mostly medium-volatility (MV) primary compounds with volatilities ranging from 10^1 to 10^2 μg m^{-3}. The corresponding model species are denoted below as LV-POA and MV-POA. The volatilities of LV-POA and MV-POA were set in our simulations at 1 and 10^2 μg m^{-3}, respectively. Note that the gas-particle partitioning of MV-POA emissions in our simulation may be similar to that of more volatile organic species, since small but dense BB plumes are effectively diluted over the size of a grid cell. Box model simulations performed with varying initial size and density of a BB plume indicated that such artificial dilution can unrealistically enhance SOA formation (Konovalov et al., 2019). For these reasons, the BB emissions of SVOCs species with a volatility of ~10^3 μg m^{-3} are assumed to be also represented by MV-POA. The fire emissions of

POA were split between LV-POA and MV-POA species based on a ratio of 4 to 3 following the estimates by May et al. (2013).

In our simulations, we merged the two SOA sets that had been originally introduced in C17. Similar to primary organic compounds, secondary compounds with volatilities lower than or equal to 1 μg m^{-3} are aggregated as one model species, LV-SOA. To allow for a more realistic representation of the multi-generation aging of SOA, we retained a distinct SOA species with relatively high volatility (HV) of 10^3 μg m^{-3}. Our scheme also involves an MV-SOA species with a volatility of 10^2 μg m^{-3}. The POA and SOA species were given the same molecular weight as their respective analogs from the second, fourth, and fifth volatility classes of the SVOC sets 1 and 3 from the original C17 scheme. The properties of the VBS species in our model are listed in Table 1.

The reactions representing the evolution of BB OA within our simplified VBS scheme are specified in Table 2. Specifically, the POA species in the gas phase are assumed to undergo reactions (R1) and (R2), where the stoichiometric factor of 1.3 is introduced to account for the difference between the molecular weights for SOA from the second volatility class of set 2 of the C17 scheme and the merged SOA set in our model (189 and 144 g mol^{-1}, respectively). Following C17, we assume that apart from the oxidation of POA, SOA species are produced from the oxidation of NTVOCs (see reaction (R3)). However, we simplified the SOA yields: the direct oxidation of NTVOCs is assumed to result in the formation of only HV-SOA and LV-SOA, while the formation of MV-SOA is disregarded. The SOA yields for HV-SOA and LV-SOA are defined to retain the same total yield of SOA mass from the oxidation of NTVOCs as in C17 (~ 43 g mol^{-1}). The value of the stoichiometric parameter ξ_1 determining HV-SOA and LV-SOA yields was varied in our test simulations to enable consistency of our simulations with the satellite observations considered (see Sect. 2.6). The simulation results presented in this paper were obtained with ξ_1 equal to 0.85.

Oxidation of gas-phase HV-SOA is assumed to yield MV-SOA (reaction R4). Since the molecular weight of MV-SOA is larger than that of HV-SOA (see Table 1), functionalization is presumed to effectively dominate – although only slightly – over fragmentation in the oxidation of "high-volatility" organic species. However, fragmentation is assumed to dominate over functionalization in the oxidation of both MV-SOA and LV-SOA in (R5) and (R6): the reaction yield is controlled by another adjustable parameter, ξ_2, which is set in our simulations at the small value of 0.15 (see Sect. 2.6 for the adjustment procedure). This means that OH oxidation of MV-SOA and LV-SOA yields 15% of LV-SOA by a functionalization pathway, while the fragmentation pathway accounts for 85% of products, which are considered as volatile and do not contribute to SOA formation. A lower volatility of the SOA species is associated with a higher O:C ratio (see C17), thus making less volatile species more prone to fragmentation. The reaction rates (k_{OH}) for reactions (R1)-(R4) are taken to be the same as those for similar reactions in C17, but a smaller rate is set for reactions (R5) and (R6), presuming that they represent multi-generation fragmentation processes.

One more adjustable parameter – ξ_3 – in our simplified VBS scheme is the emission ratio of the mass concentration of NTVOCs to the sum of mass concentrations of the POA species, which was set at 14.2. The same parameter was estimated in C17: its optimal value was found to be 4.75 (that is, three times less than in our case), although a much larger value (up to 9.8) was found to be also consistent with the measurements analyzed in C17. As noted above, the results of the experiments performed in C17 do not directly apply to the case of BB aerosol from Siberian fires. Hence, it does not seem infeasible that oxidation of VOC emissions from Siberian fires indeed effectively yields more SOA than oxidation of VOCs from the combustion of beech logs.

Enthalpies of vaporization (ΔH_{vap}) of the surrogate OA species are evaluated using the estimates derived by May et al. (2013) from thermodenuder measurements of fresh BB aerosol. The same ΔH_{vap} values (depending on the volatility) are used both for POA and SOA species.

The optical properties of BB aerosol particles (for both ‘bb_vbs’ and ‘bb_trc’ scenarios) are evaluated using the OPTSIM software (Stromatas et al., 2012) under the assumption that any particle is composed of a spherical BC core surrounded by a concentric shell consisting of homogeneously mixed organic components, inorganic salts and water. Given the simulated size-resolved mass concentration and composition of BB aerosol particles, as well as the complex refractive index for each particle component, the scattering and absorbing efficiencies for the particles are computed for the core-shell mixing scenario with a Mie code based on the formulations proposed by Toon and Ackerman (1981). The scattering and absorption efficiencies are then used to compute both the AOD and AAOD values. Note that Mie core/shell models in which a BC core is represented as a perfect sphere have been found to be prone to underestimation of the fractional contribution of BC to absorption at near-UV wavelength in cases where the coating is relatively thin (with the shell/core mass ratio less than 3) as a result of the fact that actual BC particles are typically non-spherical aggregates (Liu et al., 2017; Taylor et al., 2020). However, this potential underestimation is unlikely to be significant in our simulations representing typical Siberian BB aerosol, which features typical OC/ BC mass ratios as large as almost 30 (Mikhailov et al., 2017).

The real part of the refractive index for all of the BB aerosol components resolved in our simulation (see Sect. 2.3), as well as the imaginary part of the refractive index for the inorganic components (including BC), were taken in our computations to be the same as those given in Stromatas et al. (2012) for the 532 nm wavelength (see Table 3 therein) and are assumed for simplicity to be the same for both the 388 and 550 nm wavelengths considered here. In the ‘bb_trc’ simulation, BB aerosol absorption was calculated under the assumption that the organic shell is non-absorbing. Evaluation of the imaginary part of the refractive indexes for the POA and SOA species, k_{poa} and k_{soa}, in our simulations for the ‘bb_vbs’ scenario involved the following assumptions.

First, based on the experimental findings (Saleh et al., 2014) that almost all BrC absorption of fresh BB aerosol is associated with extremely low-volatility organic compounds, we assumed that MV-POA is not absorbing. Based on the estimates of the imaginary refractive index of fresh OA, k_{OA}, and their uncertainties, which have been reported by Lu et al. (2015) as a function of the BC-to-OA ratio, and assuming an average value of the BC-to-OC ratios for Siberian BB aerosol to be about 0.04 (Mikhailov et al., 2017; Konovalov et al., 2017b), we conservatively estimated k_{OA} to be 0.013. This estimate, which is in the lower range of the corresponding k_{OA} values ($k_{OA} \approx 0.025 \pm 50\%$) given by Lu et al. (2015), is expected to ensure that the contribution of POA to BB aerosol absorption in our simulations is not overestimated. Accordingly, taking into account the assumed MV-POA / LV-POA emission ratio (see above), we estimated k_{poa} (for LV-POA) to be 0.03.

Second, we assumed that, as a result of UV photodegradation, k_{poa} decreases exponentially with the BB aerosol photochemical age (t_e). Taking into account the laboratory results by Fleming et al. (2020), we assumed the lifetime of BrC chromophores in the LV-POA species to UV photodegradation to be 82 h. This lifetime represents the lowest part of the range of the experimental values reported by Fleming et al. (2020, see Table 3 therein).

Third, we assumed that in contrast to POA, the low-volatility SOA, LV-SOA, is not absorbing. This assumption is not based on any direct experimental findings. However, if low-volatility SOA remaining after more rapid atmospheric processing of higher-volatility SOA would be strongly absorbing, it would be difficult to explain an almost total loss of BrC absorption of aging BB aerosol (Forrister et al., 2015), in which POA is typically replaced by oxidized species (e.g., May et al., 2015). While oxidation of low-volatility POA is likely to yield absorptive components (Wong et al., 2017), chemical processing of LV-POA in our simulations is very slow (as shown below), and so the corresponding source of BrC is disregarded. For simplicity, the HV-SOA and MV-SOA species are assumed to have the same constant value of the imaginary refractive index, k_{soa}. This value was adjusted in our simulations for the 'bb_vbs' scenario (see Sect. 2.6) and is taken to be equal to 0.009 for the 388 nm wavelength. Photochemical processing of HV-SOA and MV-SOA resulting in formation of non-absorbing LV-SOA implicitly accounts in our simulations for the destruction of BrC chromophores through all possible mechanisms, including gas-phase and heterogeneous oxidation and UV photodegradation. To the best of our knowledge, estimates of the imaginary refractive index for SOA formed from photo-oxidation of BB emissions have so far been reported only by Saleh et al. (2013) based on the analysis of smog chamber experiments. According to these estimates, the imaginary refractive index (at 388 nm) for SOA is at least 0.04 (as in the case of SOA from pocosin pine) or even much larger. However, these estimates correspond to a very initial stage of BB aerosol aging (when the UV exposure time is less than 1.5 hours), which is not addressed in our analysis, and therefore maybe not applicable to the more oxidized SOA compounds that are probably dominating aged BB aerosol particles.

Overall, except for a slow degradation of BrC by UV in primary aerosol particles, we assume that each molecule of any given SVOC species contains a constant fraction (that can be different for different species) of chromophores and that atmospheric evolution of BrC within BB aerosol particles is determined by the condensation or evaporation of the different primary and secondary organic compounds forming BB aerosol particles. This approach allows us to parameterize the evolution of the optical properties of BB aerosol within the CTM and the evolution of its chemical composition in a consistent way.

To characterize the effects of water uptake by BB aerosol particles on our computations of their optical properties, we evaluated the hygroscopicity parameter κ_{org} (Petters and Kreidenweis, 2007) for BB OA by assuming that all the SOA species feature a constant hygroscopicity parameter, κ_{org} (Petters and Kreidenweis, 2007), of 0.2 and that the POA species are hydrophobic. The chosen value of κ_{org} for SOA is representative of the mid-range of the set of κ_{org} measurements for oxidized organic compounds generated in a flow reactor (Lambe et al., 2011). Also, we took into account the water uptake by inorganic salts using the equilibrium concentrations calculated in CHIMERE with the ISORROPIA module (Nenes et al., 1998).

Finally, we would like to emphasize once again that our simplified parameterization of the physical, chemical, and optical properties of BB aerosol is not aimed at a quantitatively accurate representation of the actual very complex processes. We believe that a quantitatively accurate representation of the BB aerosol properties and their evolution in CTMs is presently not feasible in a general case due to the lack of the necessary observational constraints. However, we consider our study as a step forward towards the development of a simple and robust but yet physically sound parameterization ensuring adequate simulation of BB aerosol properties and evolution in chemistry transport and climate models.

2.5 Pre-processing and harmonization of the satellite and model data

At the preparatory stage of our analysis, the Level-2 (orbital) AAOD, AOD, and CO satellite data were projected onto the model grid with an hourly temporal resolution (corresponding to the temporal resolution of the output data from CHIMERE). Different pixels falling into the same grid cell were averaged. To select a particular AAOD retrieval among those corresponding to the different altitudes of the aerosol center mass (see Sect. 2.2), the altitude of an observed BB plume was estimated using the mass concentration of the total particulate matter from the CHIMERE simulations for the “bb_vbs” scenario. In this way, we harmonized the OMI AAOD retrievals with the corresponding simulations (similar to Zhang et al. (2015) and Konovalov et al. (2018)). As noted in Sect. 2.2, we also used the “final” AAOD retrieval product, which is not affected by possible errors of our model, but still maybe not free of biases due to differences between the actual and assumed “climatological” heights of the BB plumes.

For our analysis of EnR_{abs} or EnR_{ext}, the MODIS and IASI observations collocated – at the scale of a model grid cell – with the OMI observations were selected by requiring that the absolute value of the time difference between the measurements taken by OMI and MODIS as well as by OMI and IASI is as small as possible and does not exceed two hours. The observed BB plumes are assumed to be mostly of a large spatial scale (tens of km) and slowly evolving at a scale of a few hours. Accordingly, the temporal and spatial inconsistencies between the different satellite data are expected to result mostly in random uncertainties in our estimates of the EnR_{abs} or EnR_{ext}, which can be taken into account by the corresponding confidence intervals. For the ancillary analysis that does not involve the OMI AAOD observations (which are much sparser than the MODIS AOD and IASI CO observations), we matched only the available AOD and CO observations, again requiring that the absolute value of the time difference between these observations does not exceed 2 hours.

The simulated AAOD, AOD, and CO data were matched in both space and time to the corresponding satellite data. The simulated 3-D concentration fields of CO were first processed to compute the total CO columns using the IASI averaging kernels as described in Konovalov et al. (2014; 2016). As an additional step towards the harmonization of the satellite and simulation data, we introduced a selection criterion for the simulated data, which accounts for the fact that the OMI AAOD data considered in this study are representative only of the scenes strongly affected by fire emissions. In the framework of

https://doi.org/10.5194/acp-2020-591
Preprint. Discussion started: 29 June 2020

the OMAERUV retrieval algorithm (Torres et al., 2013), such scenes were selected based on real-time AIRS (Atmospheric Infrared Sounder) retrievals of CO. However, due to errors in the fire emissions and computations of the air pollution transport, the observed "hot spots" in the CO columns do not necessarily correspond to similarly elevated values in the simulated CO columns, AAOD, and AOD. Such a mismatch between the OMAERUV data and simulations can result in systematic biases in estimates of EnR_{abs}. To avoid these possible biases, both CO columns from the satellite observations and simulations matched in space and time were first arranged (independently) with respect to magnitudes of the total CO columns. Then, we selected only those simulations that have the same ranks as the subset of CO observations matching (as described above) the OMI AAOD data. An advantage of this selection procedure is that it does not involve any subjective quantitative criteria and its outcome is rather insensitive to the mean level of the CO fire emissions in the model. Finally, some outliers (too large and too small values of EnR_{abs} and EnR_{ext}) were removed using the three-sigma rule. Applying all the selection criteria left us with a sufficiently large number (1156) of data points (in the main data set) suitable for our statistical analysis using the method outlined in Sect. 2.2. As the OMI SSA retrievals are very sparse compared to the AAOD retrievals, we did not apply any selection criteria to the SSA data except for the common spatial and temporal windows.

Figure 2 illustrates the "ancillary" (see above) data sets of AOD observations and simulations. In addition, Figure S1 in the Supplementary Material shows similar data for the CO columns. More specifically, these figures show the AOD and CO spatial distributions averaged over the analysis period (15-31 July 2016) in comparison to the similar distributions for the preceding period (15 June -14 July 2016) when there were no strong fire emissions in the study region. These figures also introduce two special regions used in our analysis, one of which (referred to below as the "source" region) includes the locations of major Siberian fires that emitted BB plumes transported afterward to the Eastern European part of Russia and is expected to contain relatively fresh BB aerosol, and another (referred to below as the "receptor" region), which is expected to represent aged BB aerosol. The spatial distributions shown indicate that the Siberian fires caused strong enhancements of the concentrations of BB aerosol and CO in the troposphere over a big part of Eastern Europe, which is further discussed in Sect. 3.

A final step of our procedure aimed at harmonizing the satellite and simulation data involved the estimation of probable biases in the background values of CO columns and AOD. (It may be useful to recall that the background part of AAOD is neglected in our analysis.) Similar to our previous studies mentioned above, these biases were estimated by averaging the differences between the simulated and observed data representative of background conditions. A given scene was assumed to be representative of the background conditions with respect to a given characteristic (CO columns or AOD) if a corresponding simulated value for the 'fires' scenario did not exceed 10 % of the respective value for the 'bgr' scenario. In this study, the averaging is done over the period from 15 June to 15 August 2016 separately for the source region, the receptor region, and the rest of the study region. The estimated biases are then applied to the simulations of AOD and CO columns for the corresponding regions under the 'bgr' scenario.

https://doi.org/10.5194/acp-2020-591
Preprint. Discussion started: 29 June 2020

2.6 Adjustment of the model parameters

As explained above (see Sect. 2.4), our model representation of the BB aerosol aging processes for the 'vbs' scenario involves the three adjustable parameters, ξ_1-ξ_3, controlling the evolution of the POA and SOA species, and the imaginary refractive index, k_{soa}, controlling the absorptive properties of SOA. Besides, we need to adjust correction factors, F_s (see Sect. 2.3), specifically those controlling the fire emissions of BC, POA and CO. Note that the correction factor for CO emissions, F_{CO}, is applied to the emissions of all other gaseous species, except for those of NTVOCs (which were determined by scaling the POA emissions).Taking into account that AAOD for BB aerosol in Siberia is typically an order of magnitude smaller than AOD (e.g., Konovalov et al., 2018), we expected that the modeled evolution of AOD is not sensitive to k_{soa} and also not sensitive to the correction factor for BC emission, F_{BC}. Therefore, the parameters ξ_1-ξ_3, as well as the correction factors for the POA and CO emissions from fires, can be adjusted independently of k_{soa} and F_{BC}. Specifically, we required that the nonlinear trend (see Eq. 5) in EnR for the simulated AOD be consistent with the corresponding nonlinear trend in the MODIS observations:

$$\left|y_{ext}^{obs}(t_e) - y_{ext}^{sim}(t_e)\right| < \Delta_{ext}^{obs}(t_e) + \Delta_{ext}^{sim}(t_e),\ \ t_e \in [t_e^{min};\ t_e^{max}], \tag{8}$$

where $y_{ext}^{obs}(t_e)$ is the approximation of EnR$_{\mathrm{ext}}$ for the AOD observations, $y_{ext}^{sim}(t_e)$ is a similar approximation for the AOD simulations, Δ_{ext}^{obs} and Δ_{ext}^{sim} are the 95% confidence intervals for y_{ext}^{obs} and y_{ext}^{sim}, respectively, and t_e^{min} and t_e^{max} are the minimum and maximum values of the photochemical age in the selected dataset.

In the presence of significant nonlinear variations of y_{ext}^{obs}, the condition given by Eq. (8) can provide sufficiently strong observational constraints to the three parameters ξ_1-ξ_3 of our VBS scheme. To optimize the fire emissions for POA by adjusting the corresponding correction factor (F_{POA}), we further required (following Konovalov et al., 2018) that the average values of the AOD simulated using an optimal value of F_{POA}, τ_{ext}^{sim}, and of the AOD derived from MODIS observations, τ_{ext}^{obs}, be approximately equal:

$$\left|\langle\tau_{ext}^{sim}\rangle - \langle\tau_{ext}^{obs}\rangle\right|\langle\tau_{ext}^{obs}\rangle^{-1} < o, \tag{9}$$

where the angular brackets denote the averaging performed over (only) the source region and analysis period, and o is the relative error, which is set to be equal to 0.05 in this study.

Similar conditions providing observational constraints to k_{soa} and F_{BC} apply to the simulations of AAOD:

$$\left|y_{abs}^{sim}(t_e) - y_{abs}^{obs}(t_e)\right| < \Delta_{abs}^{sim}(t_e) + \Delta_{abs}^{obs}(t_e),\ \ t_e \in [t_e^{min};\ t_e^{max}], \tag{10}$$

$$\left|\langle\tau_{abs}^{sim}\rangle - \langle\tau_{abs}^{obs}\rangle\right|\langle\tau_{abs}^{obs}\rangle^{-1} < o. \tag{11}$$

Note that the trend $y_{abs}^{sim}(t_e)$ involved in Eq. (10) is expected to depend on both the correction factor F_{BC} and the imaginary refractive indexes k_{poa} (which is fixed) and k_{soa}. Taking into account Eq. (11), larger values of F_{BC} would require smaller values of k_{soa}. In turn, smaller values of k_{soa} would suppress the variability of $y_{abs}^{sim}(t_e)$ (which is expected to depend also on parameters ξ_1-ξ_3) and, therefore, the condition (10) would require a smaller value of F_{BC}. Such reasoning shows that if y_{abs}^{obs}

https://doi.org/10.5194/acp-2020-591
Preprint. Discussion started: 29 June 2020

exhibits significant changes with t_e, then the conditions (10) and (11) allow constraining each of the two parameters, k_{soa}, and F_{BC}, independently. As argued above, a similar conclusion applies to the parameters controlling the simulations of AOD.

It should be noted that Eqs. (8)-(11) do not imply a rigorous minimization procedure, but rather impose only approximate constraints on the parameters. Indeed, constraining the six parameters controlling our simulations of AAOD and AOD within the VBS framework is a challenging (even though not infeasible) computational task. On the other hand, the relatively "loose" constraints defined above allowed us to adjust the parameter values with a reasonable accuracy manually by running the model multiple times and iteratively varying the parameter values using the trial-and-error method. More specifically, starting from a priori estimates of F_{POA} and F_{BC} based on our previous studies and estimates of ξ_1-ξ_3 based on Ciarelli et al. (2017), we first adjusted the parameters ξ_1-ξ_3 and F_{POA} in an iterative process. At the next iteration cycle, using the optimized values of ξ_1-ξ_3 and F_{POA}, we adjusted the parameters k_{soa} and F_{BC}. These iteration cycles were repeated to ensure the consistency of all the parameters.

A similar but much simpler optimization procedure was realized in the case of the simulations with the standard version of CHIMERE (that is, for the 'bb_trc' scenario). Specifically, the parameters of the VBS scheme did not need to be adjusted by definition, and only a pair of iterations was needed to adjust the correction factors F_{POA} and F_{BC} under conditions (9) and (11). The CO emissions from fires were optimized in the same way as the POA and BC emission for the 'bb_trc' scenario.

The optimized values for ξ_1-ξ_3 and k_{soa} are indicated above in Sect. 2.4. The optimized values of F_{POA} and F_{BC} were found to be 2.8 and 2.9, respectively, for the 'bb_trc' scenario. These values are within the range of uncertainties of the similar estimates reported in Konovalov et al. (2018) and yield a mean ratio of BC and OC mass concentrations of about 0.05, which is rather close to the average value (0.038) of the highly variable BC/ OC ratios observed for BB aerosol in central Siberia (Mikhailov et al., 2017). For the 'bb_vbs' scenario, the optimized value of F_{POA} was found to be equal to 0.9 – that is, it is much smaller than that for the 'bb_trc' scenario. This difference accounts for the strong SOA formation in our simulations, qualitatively consistent with similar findings from our previous studies (Konovalov et al., 2015, 2017a) and with underestimation of AOD by simulations in which SOA formation was treated as a minor process (e.g., Petrenko et al., 2012; Tosca et al., 2013; Reddington et al., 2016). The optimized value of F_{BC} (1.5) is also found to be smaller than for the 'bb_vbs' scenario, indicating a significant contribution of BrC to BB aerosol absorption. With this factor, the 'bb_vbs' simulation yields a mean ratio of BC and OC mass concentrations of 0.035, which is a quite realistic value, given the aforementioned observations by Mikhailov et al. (2017) and estimates by Konovalov et al. (2017b). This fact indicates that the absorption closure carried out in our numerical experiments is sufficiently adequate. A higher BC content in our 'bb_trc' simulation than in the 'bb_vbs' one compensates for the BrC absorption, which is not taken into account in the 'bb_trc' simulation. The F_{CO} factor was set to 1.9 for both 'bb_vbs' and 'bb_trc' scenarios.

https://doi.org/10.5194/acp-2020-591
Preprint. Discussion started: 29 June 2020

3 Results

3.1 Analysis using the two-region approach

In this section, we provide some preliminary characterization of the input data for our analysis and examine the aging-driven changes in the optical properties of BB aerosol by considering the satellite and simulated data for the two regions ("source" and "receptor") introduced above (see Sect. 2.5 and Fig. 2). The source region includes locations of major Siberian fires, and the receptor region was affected by the aged BB plumes transported from the source region (see Fig. 2 and S1). The time series corresponding to Figs. 2 and S1 (which are based on the ancillary dataset) are presented and discussed in the Supplementary Material (Sect. S2, Figs. S2 and S3). Here we only note that the simulations taking fire emissions into account are found to be in good agreement with the observations, with the correlation coefficient exceeding 0.85.

The analysis presented in this section allows us to get some preliminary insights into the effects of atmospheric aging on the BB aerosol optical properties. The advantage of this analysis is that it does not rely on any quantitative estimates (which may be inaccurate) of the BB aerosol photochemical age and is more "transparent" than the more general analysis presented in Sect. 3.2. However, such an analysis has serious limitations, as it can provide only crude snapshots of the evolving BB plumes and does not involve a characterization of statistical uncertainties.

The spatial distributions of the OMI AAOD observations and corresponding simulations (for the 'bb_vbs' scenario) for the study region and analysis period are shown in Fig. 3. Note again that the AAOD data analyzed in this study represent only BB aerosol. Qualitatively, these distributions are similar to the corresponding distributions of AOD and CO (see Figs. 2a,c, and S1a,c), but the data are much more sparse, especially in the receptor region. Nonetheless, both the AAOD observations and simulations show numerous "hot spots" of AAOD in the source region and are also indicative of the major outflow of BB plumes from Siberia into the European territory of Russia.

Figure 4 shows the time series of the spatially averaged AAOD values according to the OMI observations and our simulations for the 'bb_vbs' and 'bb_trc' scenarios. It should be recalled that the background AAOD values were not computed in our simulations and thus are not shown. As the OMI AAOD data representing BB aerosol are almost absent for both regions outside of the analysis period, only the data for the analysis period are presented in Fig. 4. Note that for the receptor region, there is not enough data to cover even the whole analysis period. The time series for the corresponding AOD and CO values (that were selected consistently with the AAOD observations) are also shown in Fig. 4.

It can be seen that the simulations for both 'bb_vbs' and 'bb_trc' scenarios are in a rather good agreement with the AAOD observations in the source region. In the receptor region, however, the simulations for the 'bb_trc' scenario overestimate AAOD for all four days for which the data are available and are biased high by ~22 % on average. The AOD simulations for the same scenario also tend to overestimate the observations, although the bias is smaller (~16 %). In contrast, the corresponding simulations of the CO columns are practically not biased. These results indicate that the decrease of the observed values of both AAOD and AOD in the receptor region compared to the source region cannot be fully explained by the processes (such as dilution, dry and wet deposition, and coagulation) included in the simulations for the 'bb_trc' scenario. It is noteworthy that the simulations for the 'bb_vbs' scenario, which take into account BB aerosol aging, do not exhibit any bias in the case of AOD and show only a minor negative bias of ~4 % in the case of AAOD. Note that the magnitude of the biases is not quite properly illustrated in Fig. 4a, because different "daily" points represent significantly different numbers of spatial grid cells. Overall, the analysis presented in this section indicates (i) that BB aerosol transported from the source region to the receptor region was affected by aging processes that resulted in reductions of both AAOD and AOD, and (ii) that our simulations, which have been designed to account for these processes, reproduce these reductions rather adequately.

3.2 Analysis of EnRs for the AAOD and AOD observations as a function of the BB aerosol photochemical age

The results of the application of our analysis method, which is described in Sect. 2.1, to the AAOD, AOD, and SSA data retrieved from the OMI and MODIS measurements are presented in Figure 5. Different panels show the nonlinear approximations (trends) of EnRs for AAOD and AOD (Figs. 5a and 5b) as a function of the BB aerosol photochemical age, as well as similar nonlinear approximations for the SSA values that are inferred from the OMI AAOD and MODIS AOD observations (Fig. 5c) or are available directly from the OMAERUV data product (Fig. 5d). Along with the nonlinear trends for EnRs and SSA, we show the running averages over each corresponding 15 data points (for EnRs or SSA) that were preliminarily arranged with respect to the BB aerosol photochemical age. The averaging is done for illustrative purposes, as the scatter of the original data points is typically large at the scale of the trends. Note that in the special situation addressed in this study, there is a strong association between the photochemical age of BB aerosol and the geographical location (specifically, the longitude) of the BB plumes transported westward (see Fig. 6). In particular, the BB aerosol photochemical age ranges from 6 to 42 hours in the source region and from 70 to 106 hours in the receptor region. This association facilitates the interpretation of the results of our analysis and also confirms the reliability of our model estimates of the BB aerosol photochemical age.

The nonlinear trend for AAOD (Figs. 5a) reveals a statistically significant decrease in EnR_{abs} (up to ~45%) corresponding to the photochemical age (t_e) period from about 25 to 60 hours. The changes in $\mathrm{EnR}_{\mathrm{abs}}$ corresponding to both fresher and older BB aerosol are not statistically significant. This trend indicates that if AAOD were simulated for the given situation without taking into account any BB aging processes (except for coagulation) and were fitted to the AAOD observations corresponding to BB aerosol aged less than 40 h, the simulated AAOD corresponding to the aged BB plumes (t_e > 60 h) would be overestimated by ~30%. This rough estimate is in tentative agreement with the results from the two-region analysis discussed above (see Fig. 4), taking into account the ranges of the BB aerosol age in the source and the receptor region (see Fig. 6) and the uncertainty of the trends.

Variations in EnR for AOD ($\mathrm{EnR}_{\mathrm{ext}}$) are more pronounced (see Fig. 5b). Specifically, $\mathrm{EnR}_{\mathrm{ext}}$ increases by more than a factor of two during the initial 30 hours of the daytime evolution (since t_e of about 6 hours) but then decreases by ~40%. This non-monotonic behavior is not contradictory to the relatively minor overestimation of AOD in the receptor region in our simula-

https://doi.org/10.5194/acp-2020-591
Preprint. Discussion started: 29 June 2020

tions for the 'bb_trc' scenario, taking into account that the major part of the increase of EnR_{ext} occurs inside the source region, which includes BB aerosol with photochemical ages less than 40 h. Interestingly, the decreasing part of the trend in EnR_{ext} almost coincides in time with the decreasing part of the trend in EnR_{abs} (cf. Figs. 5a and 5b). This observation suggests that the reductions in both EnR_{abs} and EnR_{ext} may be driven by the same processes.

It is noteworthy that a similar increase (by a factor of two) in EnR for AOD as a result of atmospheric evolution of aerosol from Siberian fires was reported in our previous study (Konovalov et al., 2017a), despite the differences in the region, period and method of analysis compared to those in the present study. Furthermore, the previous analysis indicated the presence of a decreasing part in the dependence of EnR_{ext} on the BB aerosol photochemical age, but the statistical significance of that feature was not evaluated. The quantitative difference between the BB aerosol photochemical ages corresponding to the EnR_{ext} maximum (~30 h in this study and ~15 h in Konovalov et al., 2017a) may partly be due to the different definitions of the photochemical age.

It seems reasonable to expect that the major increase in EnR_{ext} in the absence of a similar strong increase in EnR_{abs} is likely to signify an increase in SSA. Figures 5c and 5d indicate that there is indeed a significant increase of SSA (at 388 nm) during the first 20-30 hours of the daytime evolution. According to the SSA estimates inferred from both the OMI AOD and MODIS AAOD data (Fig. 5c) under the assumption that the Ångström exponent is constant (see Sect. 2.2) and equal (in the given case) to 1.0, SSA increased with a decreasing rate from ~0.89 to almost 0.95 during the first 25 h and then continued to increase much more slowly, reaching a maximum after 67 h of the BB aerosol evolution. This assumption, however, may be too strong, because whatever processes might significantly affect AAOD and AOD will also likely affect the size distribution of the particles and the Ångström exponent. As an alternative, we also estimated variable values of the Ångström exponent for the 388 and 550 nm wavelengths by using the corresponding AOD from our simulations for the 'bb_vbs' scenario. The dependence of the derived SSA estimates on the photochemical age is found to be qualitatively similar to the dependence shown in Fig. 5c, although the amplitude of the SSA changes in the test case is smaller than in the base case (see Fig. S4). Importantly, a growing dependence on t_e is also found for the direct SSA retrievals (see Fig. 5d). In this case, SSA increases from about 0.9 to almost 0.94, and the increase is statistically significant. These direct SSA retrievals are, however, very sparse, resulting in a large uncertainty of the derived trend, and have not been selected consistently with the AAOD and AOD data (see Sect. 2.5). Although the inferred SSA increase associated with the BB aerosol aging may look relatively small, it can be regarded as an indication of major changes in the optical properties of BB aerosol. For example, an increase of SSA from 0.91 to 0.95 under a constant value of AAOD would result in an enhancement of the aerosol scattering of the solar radiation by almost a factor of two. Such enhancement can likely have serious implications for the radiative effects of BB aerosol.

Note that the freshest BB aerosol considered in our analysis has already been exposed to atmospheric processing for several hours. So, on the one hand, in the context of most BB aerosol aging experiments in smog chambers (e.g., Hennigan et al., 2011; Tiitta et al., 2016; Ciarelli et al., 2017) such an aerosol would be considered as already aged. On the other hand, these experiments do not usually examine changes in BB aerosol optical properties, especially at the long time scales addressed in this study. Therefore, a comparison of the results of our analysis with available results of laboratory experiments is not straightforward, and it goes beyond the scope of this study. However, the increase of SSA in our analysis is qualitatively consistent with the persistent enhancements of SSA of BB aerosol particles after 24 hours of atmospheric aging according to a recent analysis of AERONET data (Shi et al., 2019). Significant increases of the BB aerosol mass scattering efficiency and SSA as a result of the BB aerosol aging were observed by Kleinman et al. (2020) in near-field observations of BB plumes, consistent with an earlier observation (Akagi et al., 2012) of a major increase in aerosol light scattering in BB plumes.

In addition to the analysis outlined above, we performed several sensitivity tests aimed at examining possible systematic errors in the estimated nonlinear trends. An overview of these tests and the corresponding results is presented in the Supplementary Material, Sect. S3. The results of the tests overall confirm the robustness of our major findings discussed above.

3.3 Interpretation of the inferred changes in the BB aerosol optical properties

In this section, we employ our simulations with the CHIMERE CTM to interpret the qualitative features of the BB aerosol evolution inferred from the satellite observations. It should be noted that our interpretation is not unambiguous, especially with respect to the quantitative aspects of the effects considered. However, to the best of our knowledge, this interpretation is the first attempt to reconcile the major changes in both absorption and scattering characteristics of BB aerosol due to multi-day atmospheric aging with the available knowledge on the atmospheric transformations of BB aerosol by using numerical simulations with a CTM. The analysis presented below may have implications for developing adequate and robust parameterizations of BB aerosol aging processes in chemistry transport and climate models.

Figure 7 shows the nonlinear approximations for the AAOD and AOD enhancement ratios calculated using the simulations for the ‘bb_vbs” scenario. The corresponding approximations based on the analysis of the satellite data are also shown for comparison. Evidently, based on the criteria given by Eqs. (8) and (10), EnR_{abs} and EnR_{ext} from the simulations are overall consistent with their counterparts from the observations (see Fig. 5a, b). This fact gives credence to the representation of the BB aerosol evolution in our model.

Further insights into the processes leading to the nonlinear trends in EnR_{ext} and EnR_{abs} according to our simulations are provided by the results presented in Figs. 8-10. Specifically, Fig. 8 illustrates the evolution of the chemical composition of BB aerosol in the simulations for the ‘bb_vbs’ scenario, presenting the fractional contributions of the model species in the mass columnar concentration of BB aerosol (Fig. 8a) and the normalized EnRs for the columnar concentrations of organic species in the particulate phase (Fig. 8b). These EnRs were evaluated similar to Eq. (1) as the normalized ratio of the columnar concentration of the given component originating from fires to the columnar concentration of BB BC (which was considered as a passive tracer). Figure 8b also presents the evolution of EnR for OA in the sixth section (310-630 nm) of the particle size distribution assumed in our simulations. Figure 9 shows the evolution of the mass absorption and mass scattering efficiencies, and Fig. 10 demonstrates several sensitivity tests (explained below) aimed at a better understanding of the factors governing the evolution of EnR_{abs}. Additionally, several characteristics that can affect the gas-particle partitioning and oxidation processes and AAOD and AOD enhancement ratios are discussed in Sect. S4 (see also Fig. S8).

According to Fig. 8a, the BB aerosol composition is dominated by SOA species from the very beginning of the BB aerosol aging period addressed in our analysis (that is, from t_e bigger than about 6 h). This is not quite surprising, as the typical lifetime of NTVOCs, which is the major source of SOA in our simulations, is just ~2 hours (with k_{OH} of 4×10 cm^3 $molec^{-1}$ s^{-1} and OH concentration of ~4×10^6 cm^{-3}, see Fig. S8b). The same lifetime is characteristic for the gaseous fractions of POA (but note that the gaseous fraction of LV-POA is relatively very small) and HV-SOA. During the next 30 h or so, the remains of MV-POA and HV-SOA are evaporated and converted into LV-SOA and MV-SOA. At this stage, the SOA fraction remains nearly constant (~78 %), as the effects of evaporation and fragmentation are overall counterbalanced by the effects of condensation and functionalization. It is worth noticing, however, that while the MV-SOA fraction also remains nearly constant, the LV-SOA fraction increases by more than 20 %, and the ratio of the LV-SOA and LV-POA fractions increases very significantly by about 45 %. After about 40 h, the main processes governing the evolution of SOA are the evaporation (facilitated by dilution, see Fig. S8c) of MV-SOA, its subsequent conversion into LV-SOA, and a relatively slow evaporation and gas-phase fragmentation of the latter. Consequently, the MV-SOA fraction shrinks from 44 % to merely 5 %, whereas the LV-SOA fraction increases twofold. Following the increase of the relative humidity (see Fig. S8a) from about 40 to 65 %, the inorganic fraction (including water) also increases but still remains relatively small, contributing a maximum of 20 %.

Consistent with the results shown in Fig. 8a, the EnRs for both MV-POA and HV-SOA are rapidly decreasing and become negligible after about 60 h (see Fig. 8b). In contrast, the EnR for LV-SOA exhibits a growing tendency during the whole period of evolution, increasing by ~70 %, although becoming nearly stable after about 70 h. A growing tendency is also manifested in the evolution of the EnR for MV-SOA and total OA, but only during the initial 25 hours, after which the EnRs for both MV-SOA and total OA start to decrease. Since the BB OA concentration is typically much higher than 1 $\mu g\ m^{-3}$ (see Fig. S8c), LV-POA evaporates slowly, with its EnR decreasing by 30 % during the whole analysis period. The evaporation of LV-POA can be mainly driven by the loss of its gas phase-fraction due to reaction (R2).

It may be puzzling why EnR_{ext} is increasing twofold in the period until 30 h (see Fig. 7b), whereas no similar strong increase is demonstrated by the EnRs for any of the organic species. However, Fig. 8b also shows that the EnR for OA in particles with sizes from 310 to 630 nm increases more than three times during the same period when EnR_{ext} increases twofold. According to Mie theory, this section corresponds to the particle diameters with the maximum scattering and extinction efficiencies at 550 nm. Hence, it is not surprising that the gain of mass by particles in this section of the accumulation mode results in an enhancement of AOD. Furthermore, Fig. 9 shows that the mass scattering efficiency (which is the main contributor to the mass extinction efficiency in our case) at the 550 nm wavelength increases by a comparable amount (almost by 70 %) in the same initial period of evolution. A similar, although relatively smaller, increase (~ 25 %) takes place in the mass scattering efficiency at 388 nm. In contrast, the mass absorption efficiency at 388 nm (also shown in Fig. 9) gradually decreases during the whole period of the evolution. Therefore, according to our simulation, the changes in the mass scattering and absorption efficiencies are the key drivers for the increases in both EnR for AOD at 550 nm and SSA at 388 nm. Our further analysis indicates that the changes in the mass absorption and scattering efficiencies are indeed associated with changes in the size distribution of BB particles. Specifically, the particle size distribution shifts toward larger particles (see Fig. S9) as the BB aerosol ages. Such a shift is apparently due to a complex interplay between the evaporation process (affecting predominantly smaller particles having a larger surface-to-volume ratio) and the condensation process (that can significantly affect also bigger particles, especially in the situation when smaller particles are partially evaporated).

As could be expected, the simulated evolution of EnR_{abs} is also found to be driven by condensation and evaporation processes, but the impact of these processes on EnR_{abs} is mediated by several additional factors. In particular, one should take into account that AAOD is determined by BC, POA, and SOA species, each of which is characterized by a different value of the imaginary refractive index, and therefore equal relative changes in the mass concentrations of these components will have different impacts on AAOD. Furthermore, changes in the POA and SOA mass concentrations can affect AAOD through the lensing effect (Lack et al., 2010). To examine these factors, we ran the OPTSIM module for several limiting cases representing different optical properties of the individual components of BB aerosol simulated within the ‘bb_vbs” scenario. The main results are presented in Fig. 10, where the evolution of EnR_{abs} simulated under the different assumptions is compared with the corresponding trends derived from the OMI observations. Based on these results, we also evaluated the relative contribution of several factors to the BB aerosol absorption (see Sect. S5 and Fig. S10).

Specifically, Fig. 10a shows the trend in EnR_{abs} for the sensitivity test where the refractive index of the shell of BB particles approaches that of ambient air. This is a rather trivial case, because the size distribution of BC particles should not be affected by evaporation and condensation of the POA and SOA species, and therefore AAOD associated with such particles is expected to behave almost as an inert tracer. And indeed, EnR_{abs} computed for this case is found to be nearly constant (Fig. 10a). A minor increase in the EnR_{abs} is likely due to different effects of dry deposition and coagulation on the size distribution of BB aerosol particles in the ‘bb_vbs’ and ‘bb_trc’ scenarios. Despite being rather trivial, this test confirms the integrity of our simulations and indicates that evolution of AAOD in our simulations is almost fully determined by transformations of the organic fraction of BB aerosol. Note that in this case, the average AAOD in the selected dataset is much lower than in the base case: we estimated that “pure” BC (without the lensing effect) accounts on average for only 31% of the total absorption (see Sect. S5).

Figure 10b presents results for the opposite sensitivity test, where the contribution of BC to the BB aerosol absorption was disregarded. In other words, AAOD was computed under the assumption that BC is not absorbing. In this case, the evolution of EnR_{abs} is similar to that in the base case (see Fig. 7a), except that the amplitude of a variation of the nonlinear approximation is much larger in the test case. This test case further confirms a pivotal role played by OA in the simulated evolution of AAOD. As could be expected, constant BC absorption (see Fig. 10a) dampens, to a significant extent, the AAOD changes caused by the OA.

In principle, one would expect also that variations of the thickness of the organic shell, which are associated with the evolution of $\mathrm{EnR_{ext}}$, lead to changes in $\mathrm{EnR_{abs}}$ due to the lensing effect associated with the non-absorbing fraction of OA. To test this possibility, we set the imaginary refractive index for both POA and SOA to zero. The results of the corresponding computations are shown in Fig. 10c. According to these results, the lensing effect does not significantly contribute to the $\mathrm{EnR_{abs}}$ variations in the base case. This can be due to the saturation of the absorption enhancement by a clear coating (Wu et al., 2018) and also due to the fact that the dilution-corrected variations of OA concentration in our simulations are rather small (see Fig. 8b).

The test computations shown in Figs. 10a-10c clearly indicate that the key factor responsible for the changes of $\mathrm{EnR_{abs}}$ in our simulation is the variable BrC absorption. Further insights into the mechanism of these changes are provided by a computation under the assumption that SOA is non-absorbing (while POA is still absorbing). The results of these computations are shown in Fig. 10d. Similar to the base case, $\mathrm{EnR_{abs}}$ is decreasing with t_e, but at a much lower rate. Hence, we can conclude that the evolution of the aerosol absorption properties in our simulations is mainly driven by formation and transformations of the SOA species.

Taking the entirety of the results of our analysis into account, we suggest the following qualitative interpretation of the main processes driving the evolution of $\mathrm{EnR_{abs}}$ and $\mathrm{EnR_{ext}}$ in our simulations and, ultimately, in the real atmosphere. First, fast oxidation of NTVOCs results in production of HV-SOA and MV-SOA. HV-SOA is mostly oxidized into MV-SOA and then LV-SOA during the initial period of a few hours, which is not represented in the satellite observations considered here. Oxidation of POA provides an additional source of both MV-SOA and LV-SOA. Evaporation (and subsequent transformation) of POA and HV-SOA and formation and condensation of LV-SOA and MV-SOA leads to a major increase of $\mathrm{EnR_{ext}}$, mainly as a result of an increase in the mass scattering efficiency at 550 nm due to a shift of the size distribution towards bigger particles. In contrast, the mass absorption efficiency at 388 nm is not strongly affected by the indicated processes, and there is only a minor increase in $\mathrm{EnR_{abs}}$, which is caused by formation of MV-SOA (as LV-SOA is assumed to be non-absorbing). As the sources of MV-SOA are depleted, its concentration decreases due to the oxidation reaction (R5). Since the fragmentation pathway is assumed to be dominating in this reaction, the depletion of MV-SOA is not compensated by production of LV-SOA; so the total concentration of the SOA species also decreases. This process can explain the decreasing stage in both the $\mathrm{EnR_{abs}}$ and $\mathrm{EnR_{ext}}$ evolution. The decrease of the total SOA concentration – and the decrease of $\mathrm{EnR_{abs}}$ and $\mathrm{EnR_{ext}}$ – slows down as the MV-SOA concentration decreases. Eventually, the BB aerosol consists predominantly of the lower volatility fractions of POA and SOA. This agrees with observations of low volatility of aged BB aerosols in field campaigns (Clarke and Kapustin, 2010; Thornberry et al., 2010; Andreae et al., 2018).

We would like to emphasize that the presented interpretation is not necessarily unique. Although – based on our knowledge – we cannot propose any plausible alternative to oxidation processes associated with SOA formation and transformation as a driving force behind the major changes in the enhancement ratios for both AOD and AAOD, our interpretation involves considerable uncertainties with respect to many important features of these processes. For example, the evolution of the mass scattering efficiency (α_s) is likely to depend on the initial size distribution of the BB aerosol particles, which may be very variable (Reid et al., 2005a). A smaller increase in α_s would need to be compensated by a larger enhancement of the OA concentration (and vice versa). This could be achieved in our simulations by assuming a larger weight for the functionalization (or, alternatively, fragmentation) pathway of the oxidation reactions. Furthermore, the evolution of POA and SOA can depend on the phase state of the particles. While we assume in our simulations that particles are liquid, the critical temperature for the transition between the liquid and glassy states of the particles is estimated to be in the range of ambient temperatures in the boundary layer over Siberia (Shiraiwa et al., 2017), being a complex function of ambient relative humidity and particle composition. Slow diffusion of organic molecules within glassy or semi-solid particles could limit gas-particle interactions but effectively expose larger amounts of SOA to gas-phase photochemical processing. Taking the phase state transition processes into account would result in significant extensions of our simplified representation of BB aerosol aging, which could not be sufficiently constrained by the available observations in Siberia. However, we believe these extensions are not likely to entail major qualitative changes in the proposed interpretation of the “observed” changes in the BB aerosol optical properties.

The evolution of the imaginary refractive index of BB aerosol is also represented in our simulation in a very simplified way. Although we differentiate between the several model species with respect to this properties, both primary and secondary real organic compounds are likely to feature a much wider spectrum of absorptive properties. Nonetheless, our interpretation will likely hold, if the low-volatility SOA species formed in the real atmosphere from VOCs and POA as a result of a long chain of oxidation processes are much less absorptive than relatively fresh (and more volatile) SOA species. This assumption is supported by field observations (Forrister et al., 2015; Selimovic et al., 2019) and numerous laboratory experiments (e.g., Browne et al., 2019; Fan et al., 2019, Wong et al., 2017; 2019) indicating an eventual bleaching of BrC in BB aerosol as a result of its exposure to the atmospheric oxidation processes and UV radiation. One more important simplifying assumption involved in our simulations concerns the evolution of the optical properties of the SOA species: as noted above, we assume that the imaginary refractive index for a given “virtual” SOA species, which represent the molecular weight and volatility of their real counterparts, does not change as long as this species exists. This assumption is obviously not true in a general case, because destruction of chromophores by UV irradiation or as a result of aqueous heterogeneous oxidation is not necessarily associated with significant changes of the volatility or molecular weight of the affected compound. However, on the one hand, there is experimental evidence noted above (Fleming et al., 2020) that direct photodegradation of BrC in BB aerosol is a slow process with a characteristic time scale of at least several days – even though this observation, strictly speaking, applies only to fresh primary BB aerosol. On the other hand, aqueous heterogeneous oxidation can hardly be a significant process in our situation, where water uptake by particles – as discussed above – is typically small, although the effect of ambient relative humidity on the atmospheric evolution of BrC in BB aerosol has yet to be investigated.

Overall, this discussion suggests that although our model representation of BB aerosol evolution involves strong assumptions (which yet need to be verified in future research), our qualitative interpretation of the inferred major changes of the optical properties of BB aerosol in Siberia is sufficiently robust and realistic. In turn, the applicability of this interpretation corroborates the reliability of our major findings from the analysis of the satellite observations.

4 Conclusions

We have presented an analytical framework designed to advance the knowledge of changes in the optical properties of BB aerosol due to its atmospheric aging by using retrievals of AAOD, AOD, and SSA from satellite observations of BB plumes. This framework includes a method to evaluate nonlinear trends in the optical properties of BB aerosol due to the oxidation and gas-particle partitioning processes at the temporal scale (typically, several days) associated with a long-range transport of BB plumes. It also involves using adjustable simulations of the sources and atmospheric evolution of BB aerosol with a chemistry transport model to reproduce and interpret the inferred trends.

We used this framework to get insights into the evolution of BB aerosol optical properties during a pronounced episode of a large-scale outflow of BB smoke plumes from Siberia towards Europe that occurred in July 2016. The analysis was based on the use of OMI AAOD and SSA retrievals combined with MODIS AOD retrievals. These retrievals were used together with BB aerosol simulations and the CO columns derived from IASI observations to evaluate the enhancement ratios (EnR) for AAOD and AOD, which allows isolating the effects of oxidation and gas-particle partitioning processes from those of other processes, including transport, deposition, and wet scavenging. The simulations were performed with the CHIMERE chemistry transport model combined with the OPTSIM module enabling evaluation of the BB aerosol optical properties under the assumption of a core-shell morphology of the particles. The OA oxidation and gas-particle partitioning processes were represented in the simulation in the framework of a highly simplified but adjustable VBS scheme. Importantly, the evolution of BrC was simulated consistently with the evolution of the POA and SOA species, based on the assumptions that the POA species are much more absorptive in the near-UV wavelength range than the SOA species and that the imaginary refractive index for a given SOA "virtual" species is constant. The EnR estimates and SSA data were analyzed as a function of model-based estimates of the BB aerosol photochemical age, which – in the situation considered – is found to be strongly associated with the geographical location of a BB plume.

We found that, while the EnR for AAOD does not change significantly during the first 20-30 hours of daytime evolution, the EnR for AOD strongly (by more than a factor of 2) increases during the same period. The increase in EnR for AOD is accompanied by a statistically significant increase in SSA. Note that the first few hours of the atmospheric evolution of BB aerosol are not covered by our analysis. Further atmospheric processing of BB aerosol (up to a photochemical age of about 100 h) is found to be associated with statistically significant decreases (of about 45 %) of EnRs for both AAOD and AOD and insignificant changes of SSA.

By adjusting the imaginary refractive indexes for the SOA species, a few parameters of the simplified VBS scheme, and the emission factors, our simulations were brought into close agreement with the observed AAOD and AOD values and with the trends in EnRs for both AAOD and AOD. The analysis of our simulation results suggests that the upward trend in EnR for AOD (which is associated with the initial increase in SSA) could be due to SOA formation and POA evaporation leading to a major increase in the mass scattering efficiency of BB aerosol through modulation of the particle size distribution. Evaporation of the semi-volatile SOA is indicated as a likely reason for the subsequent decrease of the EnR for both AAOD and AOD. We suggest that despite a highly simplified (mechanistic) character of our representation of BB aerosol our simulations, our conclusions regarding the basic factors behind the "observed" BB aerosol evolution are sufficiently robust. These factors need to be adequately taken into account in chemistry transport and climate models to ensure reliable simulations of the BB aerosol optical properties and accurate estimates of associated radiative effects, specifically in Northern Eurasia. The proposed simplified representation of BB aerosol evolution can contribute to achieving such a goal, suggesting a reasonable compromise between over-complexity unconstrained by available observations and over-simplicity leading to major biases in the simulation results.

Overall, this study has demonstrated that the presented analytical framework can be helpful in identifying and interpreting manifestations of the BB aerosol aging processes far beyond the temporal scales that can currently be addressed in aerosol chamber experiments. Although the application of the framework in the present study has been limited to a concrete episode of long-range transport of BB plumes, the proposed methods are rather general and can be used in many other studies of BB aerosol and applied to different sets of satellite data, including, for example, multi-spectral retrievals of aerosol absorptive properties from MISR (Multi-Angle Imaging Spectrometer) measurements (Junghenn Noyes et al., 2020). The framework was also shown to enable validation and optimization of model representations of BB aerosol evolution. Therefore, its future applications can help address current challenges associated with the representation of the evolution and optical properties of BB aerosol and its components in regional and global models (Shrivastava et al., 2017; Samset et al., 2018; Tsigaridis and Kanakidou, 2018; Konovalov et al., 2019).

Data availability. The OMAERUV data product (Torres, 2006), the MOD04/MYD04 (Levy and Hsu, 2015) and MYD14/MOD14 datasets (Giglio and Justice, 2015a, b) are available through the NASA Earth Data Search (https://searchearthdata.nasa.gov/, last access: 19 April 2020). The CO column amounts retrieved from the IASI measurements (Clerbaux et al., 2009) are from the ESPRI data center (http://cds-espri.ipsl.fr/etherTypo/index.php?id=1707&L=1, last access: 19 April 2020). The CHIMERE chemistry transport model (CHIMERE-2017) is available at http://www.lmd.polytechnique.fr/chimere/, last access: 20 April 2020, and the OPTSIM software is available at https://www.lmd.polytechnique.fr/optsim/, last access: 20 April 2020.

Competing interests. The authors declare that they have no conflict of interest.

Author contributions. IBK and MB designed the study. IBK also designed the method to analyze satellite observations, contributed to the analysis of satellite and model data and prepared the manuscript. MB also contributed to the discussion of

the results and to the preparation of the manuscript. NAG contributed to the analysis of satellite observations and conducted a part of the numerical experiments. MOA contributed to the discussion of the results and to the preparation of the manuscript.

Financial support. The analysis and simulations of the BB aerosol evolution was supported by the Russian Science Foundation (grant agreement no. № 19-77-20109). The development and validation of the simplified VBS scheme was performed with support from the Russian Foundation for Basic Research (grant no. 18-05-00911).

References

Agarwal, S., Aggarwal, S. G., Okuzawa, K., and Kawamura, K.: Size distributions of dicarboxylic acids, ketoacids, α-dicarbonyls, sugars, WSOC, OC, EC and inorganic ions in atmospheric particles over Northern Japan: implication for long-range transport of Siberian biomass burning and East Asian polluted aerosols, Atmos. Chem. Phys., 10, 5839–5858, https://doi.org/10.5194/acp-10-5839-2010, 2010.

Ahern, A. T., Robinson, E. S., Tkacik, D. S., Saleh, R., Hatch, L. E., Barsanti, K. C., Stockwell, C. E., Yokelson, R. J., Presto, A. A., Robinson, A. L., Sullivan, R. C., and Donahue, N. M.: Production of secondary organic aerosol during aging of biomass burning smoke from fresh fuels and its relationship to VOC precursors, J. Geophys. Res., 124, 3583–3606, https://doi.org/10.1029/2018JD029068, 2019.

Ahn, C., Torres, O., and Jethva, H.: Assessment of OMI near-U aerosol optical depth over land, J. Geophys. Res.-Atmos., 119, 2457–2473, https://doi.org/10.1002/2013JD020188, 2014.

Akagi, S. K., Craven, J. S., Taylor, J. W., McMeeking, G. R., Yokelson, R. J., Burling, I. R., Urbanski, S. P., Wold, C. E., Seinfeld, J. H., Coe, H., Alvarado, M. J., and Weise, D. R.: Evolution of trace gases and particles emitted by a chaparral fire in California, Atmos. Chem. Phys., 12, 1397–1421, https://doi.org/10.5194/acp-12-1397-2012, 2012.

Andreae, M. O., and Gelencsér, A.: Black carbon or brown carbon? The nature of light-absorbing carbonaceous aerosols, Atmos. Chem. Phys., 6, 3131–3148, https://doi.org/10.5194/acp-6-3131-2006, 2006.

Andreae, M. O., Afchine, A., Albrecht, R., Holanda, B. A., Artaxo, P., Barbosa, H. M. J., Borrmann, S., Cecchini, M. A., Costa, A., Dollner, M., Fütterer, D., Järvinen, E., Jurkat, T., Klimach, T., Konemann, T., Knote, C., Krämer, M., Krisna, T., Machado, L. A. T., Mertes, S., Minikin, A., Pöhlker, C., Pöhlker, M. L., Pöschl, U., Rosenfeld, D., Sauer, D., Schlager, H., Schnaiter, M., Schneider, J., Schulz, C., Spanu, A., Sperling, V. B., Voigt, C., Walser, A., Wang, J., Weinzierl, B., Wendisch, M., and Ziereis, H.: Aerosol characteristics and particle production in the upper troposphere over the Amazon Basin, Atmos. Chem. Phys., 18, 921-961, doi:10.5194/acp-18-921-2018, 2018.

Andreae, M. O.: Emission of trace gases and aerosols from biomass burning – an updated assessment, Atmos. Chem. Phys., 19, 8523–8546, https://doi.org/10.5194/acp-19-8523-2019, 2019.

Bekryaev, R. V., Polyakov, I. V., and Alexeev, V. A.: Role of polar amplification in long-term surface air temperature variations and modern Arctic warming, J. Clim., 23, 3888-3906, https://doi.org/10.1175/2010jcli3297.1, 2010.

Bessagnet, B., Menut, L., Curci, G., Hodzic, A., Guillaume, B., Liousse, C., Moukhtar, S., Pun, B., Seigneur, C., and Schulz, M.: Regional modeling of carbonaceous aerosols over Europe – Focus on Secondary Organic Aerosols, J. Atmos. Chem., 61, 175–202, https://doi.org/10.1007/s10874-009-9129-2, 2008.

Bian, Q., Jathar, S. H., Kodros, J. K., Barsanti, K. C., Hatch, L. E., May, A. A., Kreidenweis, S. M., and Pierce, J. R.: Secondary organic aerosol formation in biomass-burning plumes: theoretical analysis of lab studies and ambient plumes, Atmos. Chem. Phys., 17, 5459-5475, https://doi.org/10.5194/acp-17-5459-2017, 2017.

Brown, H., Liu, X., Feng, Y., Jiang, Y., Wu, M., Lu, Z., Wu, C., Murphy, S., and Pokhrel, R.: Radiative effect and climate impacts of brown carbon with the Community Atmosphere Model (CAM5), Atmos. Chem. Phys., 18, 17745–17768, https://doi.org/10.5194/acp-18-17745-2018, 2018.

Browne, E. C., Zhang, X., Franklin, J. P., Ridley, K. J., Kirchstetter, T. W., Wilson, K. R., Cappa, C. D., and Kroll, J. H., Effect of heterogeneous oxidative aging on light absorption by biomass burning organic aerosol: Aerosol Sci. Tech., 53, 663-674, doi:10.1080/02786826.2019.1599321, 2019.

Bond, T. C., Doherty, S. J., Fahey, D. W., Forster, P. M., Berntsen, T., DeAngelo, B. J., Flanner, M. G., Ghan, S., Kärcher, B., Koch, D., Kinne, S., Kondo, Y., Quinn, P. K., Sarofim, M. C., Schultz, M. G., Schulz, M., Venkataraman, C., Zhang, H., Zhang, S., Bellouin, N., Guttikunda, S. K., Hopke, P. K., Jacobson, M. Z., Kaiser, J. W., Klimont, Z., Lohmann, U., Schwarz, J. P., Shindell, D., Storelvmo, T., Warren, S. G. and Zender, C. S.: Bounding the role of black carbon in the climate system: A scientific assessment, J. Geophys. Res. Atmos., 118, 5380–5552, https://doi.org/10.1002/jgrd.50171, 2013.

Ciarelli, G., El Haddad, I., Bruns, E., Aksoyoglu, S., Möhler, O., Baltensperger, U., and Prévôt, A. S. H.: Constraining a hybrid volatility basis-set model for aging of wood-burning emissions using smog chamber experiments: a box-model study based on the VBS scheme of the CAMx model (v5.40), Geosci. Model Dev., 10, 2303-2320, https://doi.org/10.5194/gmd-10-2303-2017, 2017.

Clarke, A., and Kapustin, V.: Hemispheric aerosol vertical profiles: Anthropogenic impacts on optical depth and cloud nuclei, Science, 329, 1488-1492, https://doi.org/10.1126/science.1188838, 2010.

Clerbaux, C., Boynard, A., Clarisse, L., George, M., Hadji-Lazaro, J., Herbin, H., Hurtmans, D., Pommier, M., Razavi, A., Turquety, S., Wespes, C., and Coheur, P.-F.: Monitoring of atmospheric composition using the thermal infrared IASI/MetOp sounder, Atmos. Chem. Phys., 9, 6041–6054, https://doi.org/10.5194/acp-9-6041-2009, 2009.

Cubison, M. J., Ortega, A. M., Hayes, P. L., Farmer, D. K., Day, D., Lechner, M. J., Brune, W. H., Apel, E., Diskin, G. S., Fisher, J. A., Fuelberg, H. E., Hecobian, A., Knapp, D. J., Mikoviny, T., Riemer, D., Sachse, G. W., Sessions, W., Weber, R. J., Weinheimer, A. J., Wisthaler, A., and Jimenez, J. L.: Effects of aging on organic aerosol from open biomass burning smoke in aircraft and laboratory studies, Atmos. Chem. Phys., 11, 12049-12064, https://doi.org/10.5194/acp-11-12049-2011, 2011.

Di Lorenzo, R. A., Washenfelder, R. A., Attwood, A. R., Guo, H., Xu, L., Ng, N. L., Weber, R. J., Baumann, K., Edgerton, E., and Young, C. J.: Molecular-size-separated brown carbon absorption for biomass-burning aerosol at multiple field sites, Environ. Sci. Technol., 51, 3128–3137, https://doi.org/10.1021/acs.est.6b06160, 2017.

Donahue, N. M., Robinson, A. L., Stanier, C. O., and Pandis, S. N.: Coupled partitioning, dilution, and chemical aging of semivolatile organics, Environ. Sci. Technol., 40, 2635–2643, https://doi.org/10.1021/es052297c, 2006.

Efron, B. and Tibshirani, R. J.: An introduction to the bootstrap, Chapman & Hall, New York, 1993.

ESPRI: IASI retrievals, available at http://cds-espri.ipsl.fr/etherTypo/index.php?id=1707&L=1, last access: 15 April 2020.

Evangeliou, N., Balkanski, Y., Hao, W. M., Petkov, A., Silverstein, R. P., Corley, R., Nordgren, B. L., Urbanski, S. P., Eckhardt, S., Stohl, A., Tunved, P., Crepinsek, S., Jefferson, A., Sharma, S., Nøjgaard, J. K., and Skov, H.: Wildfires in northern Eurasia affect the budget of black carbon in the Arctic – a 12-year retrospective synopsis (2002–2013), Atmos. Chem. Phys., 16, 7587–7604, https://doi.org/10.5194/acp-16-7587-2016, 2016.

Fan, X., Yu, X., Wang, Y., Xiao, X., Li, F., Xie, Y., Wei, S., Song, J., and Peng, P., The aging behaviors of chromophoric biomass burning brown carbon during dark aqueous hydroxyl radical oxidation processes in laboratory studies: Atmos. Environ., 205, 9-18, doi:10.1016/j.atmosenv.2019.02.039, 2019.

Fleming, L. T., Lin, P., Roberts, J. M., Selimovic, V., Yokelson, R., Laskin, J., Laskin, A., and Nizkorodov, S. A.: Molecular composition and photochemical lifetimes of brown carbon chromophores in biomass burning organic aerosol, Atmos. Chem. Phys., 20, 1105–1129, https://doi.org/10.5194/acp-20-1105-2020, 2020.

Forrister, H., Liu, J., Scheuer, E., Dibb, J., Ziemba, L., Thornhill, K. L., Anderson, B., Diskin, G., Perring, A. E., Schwarz, J. P., Campuzano-Jost, P., Day, D. A., Palm, B. B., Jimenez, J. L., Nenes, A., and Weber, R. J.: Evolution of brown carbon in wildfire plumes, Geophys. Res. Lett., 42, 4623–4630, https://doi.org/10.1002/2015GL063897, 2015.

George, M., Clerbaux, C., Hurtmans, D., Turquety, S., Coheur, P.- F., Pommier, M., Hadji-Lazaro, J., Edwards, D. P., Worden, H., Luo, M., Rinsland, C., and McMillan, W.: Carbon monoxide distributions from the IASI/METOP mission: evaluation with other space-borne remote sensors, Atmos. Chem. Phys., 9, 8317–8330, https://doi.org/10.5194/acp-9-8317-2009, 2009.

Giglio, L. and Justice, C.: MOD14 MODIS/Terra Thermal Anomalies/ Fire 5-Min L2 Swath 1km V006 [Data set], NASA EOSDIS LP DAAC, https://doi.org/10.5067/MODIS/MOD14.006, 2015a.

Giglio, L. and Justice, C.: MYD14 MODIS/Aqua Therma Anomalies/Fire 5-Min L2 Swath 1km V006 [Data set], NASA EOSDIS Land Processes DAAC, https://doi.org/10.5067/MODIS/MYD14.006, 2015b.

Gorchakov, G.I., Golitsyn, G.S., Sitnov, S.A., Karpov, A. V., Gorchakova, I. A., Gushchin, R.A., and Datsenko, O.I.: Large-Scale Haze over Eurasia in July 2016, Dokl. Earth Sc., 482, 1212, https://doi.org/10.1134/S1028334X1809012X, 2018.

Guenther, A., Karl, T., Harley, P., Wiedinmyer, C., Palmer, P. I., and Geron, C.: Estimates of global terrestrial isoprene emissions using MEGAN (Model of Emissions of Gases and Aerosols from Nature), Atmos. Chem. Phys., 6, 3181–3210, https://doi.org/10.5194/acp-6-3181-2006, 2006.

Gupta, P., Doraiswamy, P., Levy, R., Pikelnaya, O., Maibach, J., Feenstra, B., Polidori, A., Kiros, F., and Mills, K. C.: Impact of California fires on local and regional air quality: the role of a low-cost sensor network and satellite observations, GeoHealth, 2, 172–181, https://doi.org/10.1029/2018GH000136, 2018.

Gustafsson, Ö., and Ramanathan, V.: Convergence on climate warming by black carbon aerosols, Proc. Natl. Acad. Sci., 113, 4243-4245, doi:10.1073/pnas.1603570113, 2016.

Hennigan, C. J., Miracolo, M. A., Engelhart, G. J., May, A. A., Presto, A. A., Lee, T., Sullivan, A. P., McMeeking, G. R., Coe, H., Wold, C. E., Hao, W.-M., Gilman, J. B., Kuster, W. C., de Gouw, J., Schichtel, B. A., Collett Jr., J. L., Kreidenweis, S. M., and Robinson, A. L.: Chemical and physical transformations of organic aerosol from the photo-oxidation of open biomass burning emissions in an environmental chamber, Atmos. Chem. Phys., 11, 7669–7686, https://doi.org/10.5194/acp-11-7669-2011, 2011.

Hobbs, P. V., and Radke, L. F.: Cloud Condensation Nuclei from a Simulated Forest Fire, Science, 163 (3864), 279–280 https://doi.org/10.1126/science.163.3864.279, 1969

Hodshire, A. L., Bian, Q., Ramnarine, E., Lonsdale, C. R., Alvarado, M. J., Kreidenweis, S. M., Jathar, S. H., and Pierce, J. R.: More than emissions and chemistry: Fire size, dilution, and background aerosol also greatly influence near-field biomass burning aerosol aging, J. Geophys. Res.-Atmos., 124, 5589–5611, https://doi.org/10.1029/2018JD029674, 2019.

Hodzic, A., Jimenez, J. L., Madronich, S., Canagaratna, M. R., DeCarlo, P. F., Kleinman, L., and Fast, J.: Modeling organic aerosols in a megacity: Potential contribution of semi-volatile and intermediate volatility primary organic compounds to secondary organic aerosol formation, Atmos. Chem. Phys., 10, 5491–5514, https://doi.org/10.5194/acp-10-5491-2010, 2010.

Hornik, K., Stinchcombe, M., and White, H.: Multilayer feedforward networks are universal approximators, Neural Networks, 2, 359-366, 1989.

Hurtmans, D., Coheur, P.-F., Wespes, C., Clarisse, L., Scharf, O., Clerbaux, C., Hadji-Lazaro, J., George, M., and Turquety, S.: FORLI radiative transfer and retrieval code for IASI, J. Quant. Spectrosc. Ra., 113, 1391–1408, 2012, https://doi.org/10.1016/j.jqsrt.2012.02.036.

Ikeda, K., and Tanimoto, H.: Exceedances of air quality standard level of PM2.5 in Japan caused by Siberian wildfires, Environ. Res. Lett., 10, 105001 , https://doi.org/10.1088/1748-9326/10/10/105001, 2015.

Jacobson, M. Z.: Effects of biomass burning on climate, accounting for heat and moisture fluxes, black and brown carbon, and cloud absorption effects, J. Geophys. Res.-Atmos., 119, 8980–9002, https://doi.org/10.1002/2014JD021861, 2014.

Janssens-Maenhout, G., Crippa, M., Guizzardi, D., Dentener, F., Muntean, M., Pouliot, G., Keating, T., Zhang, Q., Kurokawa, J., Wankmüller, R., Denier van der Gon, H., Kuenen, J. J. P., Klimont, Z., Frost, G., Darras, S., Koffi, B., and Li, M.: HTAP_v2.2: a mosaic of regional and global emission grid maps for 2008 and 2010 to study hemispheric transport of air pollution, Atmos. Chem. Phys., 15, 11411–11432, https://doi.org/10.5194/acp-15-11411-2015, 2015.

Jen, C. N., Hatch, L. E., Selimovic, V., Yokelson, R. J., Weber, R., Fernandez, A. E., Kreisberg, N. M., Barsanti, K. C., and Goldstein, A. H.: Speciated and total emission factors of particulate organics from burning western US wildland fuels and their dependence on combustion efficiency, Atmos. Chem. Phys., 19, 1013–1026, https://doi.org/10.5194/acp-19-1013-2019, 2019.

Jethva, H. and Torres, O.: Satellite-based evidence of wavelength-dependent aerosol absorption in biomass burning smoke inferred from Ozone Monitoring Instrument, Atmos. Chem. Phys., 11, 10541–10551, https://doi.org/10.5194/acp-11-10541-2011, 2011.

Jethva, H., Torres, O., and Ahn, C.: Global assessment of OMI aerosol single-scattering albedo using ground-based AERONET inversion, J. Geophys. Res.-Atmos., 119, 9020– 9040, https://doi.org/10.1002/2014JD021672, 2014.

Jiang, Y. Q., Lu, Z., Liu, X. H., Qian, Y., Zhang, K., Wang, Y. H., and Yang, X. Q., Impacts of global open-fire aerosols on direct radiative, cloud and surface-albedo effects simulated with CAM5: Atmos. Chem. Phys., 16, 14,805-14,824, doi:10.5194/acp-16-14805-2016, 2016.

Jo, D. S., Park, R. J., Lee, S., Kim, S.-W., and Zhang, X.: A global simulation of brown carbon: implications for photochemistry and direct radiative effect, Atmos. Chem. Phys., 16, 3413–3432, https://doi.org/10.5194/acp-16-3413-2016, 2016.

Jolleys, M. D., Coe, H., McFiggans, G., Taylor, J. W., O'Shea, S. J., Le Breton, M., Bauguitte, S. J.-B., Moller, S., Di Carlo, P., Aruffo, E., Palmer, P. I., Lee, J. D., Percival, C. J., and Gallagher, M. W.: Properties and evolution of biomass burning organic aerosol from Canadian boreal forest fires, Atmos. Chem. Phys., 15, 3077-3095, https://doi.org/10.5194/acp-15-3077-2015, 2015.

Junghenn Noyes, K.; Kahn, R., Sedlacek, A., Kleinman, L., Limbacher, J., and Li, Z.: Wildfire Smoke Particle Properties and Evolution, from Space-Based Multi-Angle Imaging, Remote Sens., 12, 769, https://doi.org/10.3390/rs12050769, 2020.

Keywood, M., Kanakidou, M., Stohl, A., Dentener, F., Grassi, G., Meyer, C. P., Torseth, K., Edwards, D., Thompson, A. M., Lohmann, U., and Burrows, J.: Fire in the air: biomass burning impacts in a changing climate, Crit. Rev. Env. Contr., 43, 40–83, https://doi.org/10.1080/10643389.2011.604248, 2013.

Kleinman, L. I., Sedlacek Iii, A. J., Adachi, K., Buseck, P. R., Collier, S., Dubey, M. K., Hodshire, A. L., Lewis, E., Onasch, T. B., Pierce, J. R., Shilling, J., Springston, S. R., Wang, J., Zhang, Q., Zhou, S., and Yokelson, R. J., Rapid Evolution of

Aerosol Particles and their Optical Properties Downwind of Wildfires in the Western U.S: Atmos. Chem. Phys. Discuss., 2020, 1-52, doi:10.5194/acp-2020-239, 2020.

Konovalov, I. B., Beekmann, M., Richter, A., Burrows, J. P., and Hilboll, A.: Multi-annual changes of NO_x emissions in megacity regions: nonlinear trend analysis of satellite measurement based estimates, Atmos. Chem. Phys., 10, 8481–8498, https://doi.org/10.5194/acp-10-8481-2010, 2010.

Konovalov, I. B., Beekmann, M., Kuznetsova, I. N., Yurova, A., and Zvyagintsev, A. M.: Atmospheric impacts of the 2010 Russian wildfires: integrating modelling and measurements of an extreme air pollution episode in the Moscow region, Atmos. Chem. Phys., 11, 10031–10056, https://doi.org/10.5194/acp-11-10031-2011, 2011.

Konovalov, I. B., Beekmann, M., D'Anna, B., and George, C.: Significant light induced ozone loss on biomass burning aerosol: Evidence from chemistry-transport modeling based on new laboratory studies, Geophys. Res. Lett., 39, L17807, doi:10.1029/2012GL052432, 2012.

Konovalov, I. B., Berezin, E. V., Ciais, P., Broquet, G., Beekmann, M., Hadji-Lazaro, J., Clerbaux, C., Andreae, M. O., Kaiser, J. W., and Schulze, E.-D.: Constraining CO_2 emissions from open biomass burning by satellite observations of co-emitted species: a method and its application to wildfires in Siberia, Atmos. Chem. Phys., 14, 10383–10410, https://doi.org/10.5194/acp-14-10383-2014, 2014.

Konovalov, I. B., Beekmann, M., Berezin, E. V., Petetin, H., Mielonen, T., Kuznetsova, I. N., and Andreae, M. O.: The role of semi-volatile organic compounds in the mesoscale evolution of biomass burning aerosol: a modeling case study of the 2010 mega-fire event in Russia, Atmos. Chem. Phys., 15, 13269-13297, https://doi.org/ 10.5194/acp-15-13269-2015, 2015.

Konovalov, I. B., Berezin, E. V., Ciais, P., Broquet, G., Zhuravlev, R. V., and Janssens-Maenhout, G.: Estimation of fossil-fuel CO_2 emissions using satellite measurements of "proxy" species, Atmos. Chem. Phys., 16, 13509–13540, https://doi.org/10.5194/acp-16-13509-2016, 2016.

Konovalov, I. B., Beekmann, M., Berezin, E. V., Formenti, P., and Andreae, M. O.: Probing into the aging dynamics of biomass burning aerosol by using satellite measurements of aerosol optical depth and carbon monoxide, Atmos. Chem. Phys., 17, 4513-4537, https://doi.org/10.5194/acp-17-4513-2017, 2017a.

Konovalov, I. B., Lvova, D. A., and Beekmann, M.: Estimation of the elemental to organic carbon ratio in biomass burning aerosol using AERONET retrievals, Atmosphere, 8, 122, https://doi.org/10.3390/atmos8070122, 2017b.

Konovalov, I. B., Lvova, D. A., Beekmann, M., Jethva, H., Mikhailov, E. F., Paris, J.-D., Belan, B. D., Kozlov, V. S., Ciais, P., and Andreae, M. O.: Estimation of black carbon emissions from Siberian fires using satellite observations of absorption and extinction optical depths, Atmos. Chem. Phys., 18, 14889-14924, https://doi.org/10.5194/acp-18-14889-2018, 2018.

Konovalov, I. B., Beekmann, M., Golovushkin, N. A., and Andreae, M. O.: Nonlinear behavior of organic aerosol in biomass burning plumes: a microphysical model analysis, Atmos. Chem. Phys., 19, 12091–12119, https://doi.org/10.5194/acp-19-12091-2019, 2019.

Kroll, J. H., Ng, N. L., Murphy, S. M., Flagan, R. C., and Seinfeld, J. H.: Secondary organic aerosol formation from isoprene photooxidation, Environ. Sci. Technol., 40, 1869–1877, https://doi.org/10.1021/es0524301, 2006.

Kumar, N. K., Corbin, J. C., Bruns, E. A., Massabó, D., Slowik, J. G., Drinovec, L., Močnik, G., Prati, P., Vlachou, A., Baltensperger, U., Gysel, M., El-Haddad, I., and Prévôt, A. S. H., Production of particulate brown carbon during atmospheric aging of residential wood-burning emissions: Atmos. Chem. Phys., 18, 17843-17861, doi:10.5194/acp-18-17843-2018, 2018.

Lack, D. A., and Cappa, C. D.: Impact of brown and clear carbon on light absorption enhancement, single scatter albedo and absorption wavelength dependence of black carbon, Atmos. Chem. Phys., 10, 4207–4220, https://doi.org/10.5194/acp-10-4207-2010, 2010.

Laing, J. R., Jaffe, D. A., and Hee, J. R.: Physical and optical properties of aged biomass burning aerosol from wildfires in Siberia and the Western USA at the Mt. Bachelor Observatory, Atmos. Chem. Phys., 16, 15185–15197, https://doi.org/10.5194/acp-16-15185-2016, 2016.

Lambe, A. T., Onasch, T. B., Massoli, P., Croasdale, D. R., Wright, J. P., Ahern, A. T., Williams, L. R., Worsnop, D. R., Brune, W. H., and Davidovits, P.: Laboratory studies of the chemical composition and cloud condensation nuclei (CCN) activity of secondary organic aerosol (SOA) and oxidized primary organic aerosol (OPOA), Atmos. Chem. Phys., 11, 8913–8928, https://doi.org/10.5194/acp-11-8913-2011, 2011.

Laskin, A., Laskin, J., and Nizkorodov, S. A., Chemistry of atmospheric brown carbon: Chem. Rev., 115, 4335-4382, doi:10.1021/cr5006167, 2015.

Lelieveld, J., Pozzer, A., Pöschl, U., Fnais, M., Haines, A., and Münzel, T., Loss of life expectancy from air pollution compared to other risk factors: a worldwide perspective: Cardiovascular Research, doi:10.1093/cvr/cvaa025, 2020.

Levelt, P. F., Hilsenrath, E., Leppelmeier, G. W., van den Oord, G. H. J., Bhartia, P. K., Tamminen, J., de Haan, J. F., and Veefkind, J. P.: Science objectives of the ozone monitoring instrument, IEEE T. Geosci. Remote, 44, 1199–1208, https://doi.org/10.1109/TGRS.2006.872336, 2006.

Levin, E. J. T., McMeeking, G. R., Carrico, C. M., Mack, L. E., Kreidenweis, S. M., Wold, C. E., Moosmuller, H., Arnott, W. P., Hao, W. M., Collett, J. L., and Malm, W. C., Biomass burning smoke aerosol properties measured during Fire Laboratory at Missoula Experiments (FLAME): J. Geophys. Res., 115, D18210, doi:10.1029/2009jd013601, 2010.

Levy, R. C., Remer, L. A., Kleidman, R. G., Mattoo, S., Ichoku, C., Kahn, R., and Eck, T. F.: Global evaluation of the Collection 5 MODIS dark-target aerosol products over land, Atmos. Chem. Phys., 10, 10399–10420, https://doi.org/10.5194/acp-10-10399-2010, 2010.

Levy, R. C., Mattoo, S., Munchak, L. A., Remer, L. A., Sayer, A. M., Patadia, F., and Hsu, N. C.: The Collection 6 MODIS aerosol products over land and ocean, Atmos. Meas. Tech., 6, 2989–3034, https://doi.org/10.5194/amt-6-2989-2013, 2013.

Levy, R. and Hsu, C.: MODIS Atmosphere L2 Aerosol Product. NASA MODIS Adaptive Processing System, Goddard Space Flight Center, USA, https://doi.org/10.5067/MODIS/MYD04_L2.006, 2015.

https://doi.org/10.5194/acp-2020-591
Preprint. Discussion started: 29 June 2020

Li, C., He, Q., Schade, J., Passig, J., Zimmermann, R., Meidan, D., Laskin, A., and Rudich, Y., Dynamic changes in optical and chemical properties of tar ball aerosols by atmospheric photochemical aging: Atmos. Chem. Phys., 19, 139-163, doi:10.5194/acp-19-139-2019, 2019.

Lim, C. Y., Hagan, D. H., Coggon, M. M., Koss, A. R., Sekimoto, K., de Gouw, J., Warneke, C., Cappa, C. D., and Kroll, J. H.: Secondary organic aerosol formation from the laboratory oxidation of biomass burning emissions, Atmos. Chem. Phys., 19, 12797–12809, https://doi.org/10.5194/acp-19-12797-2019, 2019.

Liu, D., Whitehead, J., Alfarra, M. R., Reyes-Villegas, E., Spracklen, D. V., Reddington, C. L., Kong, S., Williams, P. I., Ting, Y.-C., Haslett, S., Taylor, J. W., Flynn, M. J., Morgan, W. T., McFiggans, G., Coe, H., and Allan, J. D.: Blackcarbon absorption enhancement in the atmosphere determined by particle mixing state, Nature Geoscience, 10, 184–188, https://doi.org/doi:10.1038/ngeo2901, 2017.

Liu, S., Aiken, A. C., Arata, C., Dubey, M. K., Stockwell, C. E., Yokelson, R. J., Stone, E. A., Jayarathne, T., Robinson, A. L., DeMott, P. J., and Kreidenweis, S. M., Aerosol single scattering albedo dependence on biomass combustion efficiency: Laboratory and field studies: Geophys. Res. Lett., 41, 742-748, doi:10.1002/2013GL058392, 2014.

Lu, Zi., Streets, D. G., Winijkul, E., Yan, F., Chen, Y., Bond, T. C., Feng, Y., Dubey, M. K., Liu, S., Pinto, J. P., and Carmichael, G. R.: Light absorption properties and radiative effects of primary organic aerosol emissions, Environ. Sci. Technol., 49, 4868–4877, https://doi.org/10.1021/acs.est.5b00211, 2015.

Lu, Zh., Liu, X., Zhang, Z., Zhao, C., Meyer, K., Rajapakshe, C., Wu, C., Yang, Z., and Penner, J. E.: Biomass smoke from southern Africa can significantly enhance the brightness of stratocumulus over the southeastern Atlantic Ocean, P. Natl. Acad. Sci. USA, 115, 2924–2929, https://doi.org/10.1073/pnas.1713703115, 2018.

Mailler, S., Menut, L., Khvorostyanov, D., Valari, M., Couvidat, F., Siour, G., Turquety, S., Briant, R., Tuccella, P., Bessagnet, B., Colette, A., Létinois, L., Markakis, K., and Meleux, F.: CHIMERE-2017: from urban to hemispheric chemistry-transport modeling, Geosci. Model Dev., 10, 2397-2423, https://doi.org/10.5194/gmd-10-2397-2017, 2017.

Majdi, M., Turquety, S., Sartelet, K., Legorgeu, C., Menut, L., and Kim, Y.: Impact of wildfires on particulate matter in the Euro-Mediterranean in 2007: sensitivity to some parameterizations of emissions in air quality models, Atmos. Chem. Phys., 19, 785–812, https://doi.org/10.5194/acp-19-785-2019, 2019.

Marelle, L., Raut, J.-C., Thomas, J. L., Law, K. S., Quennehen, B., Ancellet, G., Pelon, J., Schwarzenboeck, A., and Fast, J. D.: Transport of anthropogenic and biomass burning aerosols from Europe to the Arctic during spring 2008, Atmos. Chem. Phys., 15, 3831–3850, https://doi.org/10.5194/acp-15-3831-2015, 2015.

Matsui, H., Koike, M., Kondo, Y., Oshima, N., Moteki, N., Kanaya, Y., Takami, A., and Irwin, M.: Seasonal variations of Asian black carbon outflow to the Pacific: contribution from anthropogenic sources in China and biomass burning sources in Siberia and Southeast Asia, J. 20 Geophys. Res. Atmos., 118, 9948–9967, https://doi.org/10.1002/jgrd.50702, 2013.

May, A. A., Levin, E. J. T., Hennigan, C. J., Riipinen, I., Lee, T., Collett Jr., J. L., Jimenez, J. L., Kreidenweis, S. M., and Robinson, A. L.: Gas-particle partitioning of primary organic aerosol emissions: 3. Biomass burning, J. Geophys. Res. Atmos., 118, 11327–11338, https://doi.org/10.1002/jgrd.50828, 2013.

May, A. A., Lee, T., McMeeking, G. R., Akagi, S., Sullivan, A. P., Urbanski, S., Yokelson, R. J., and Kreidenweis, S. M.: Observations and analysis of organic aerosol evolution in some prescribed fire smoke plumes, Atmos. Chem. Phys., 15, 6323-6335, https://doi.org/10.5194/acp-15-6323-2015, 2015.

McClure, C. D., Lim, C. Y., Hagan, D. H., Kroll, J. H., and Cappa, C. D., Biomass-burning-derived particles from a wide variety of fuels – Part 1: Properties of primary particles: Atmos. Chem. Phys., 20, 1531-1547, doi:10.5194/acp-20-1531-2020, 2020.

McMeeking, G. R., Kreidenweis, S. M., Baker, S., Carrico, C. M., Chow, J. C., Collett, J. L., Hao, W. M., Holden, A. S., Kirchstetter, T. W., Malm, W. C., Moosmuller, H., Sullivan, A. P., and Wold, C. E., Emissions of trace gases and aerosols during the open combustion of biomass in the laboratory: J. Geophys. Res., 114, D19210, doi:10.1029/2009jd011836, 2009.

Menut, L., Bessagnet, B., Khvorostyanov, D., Beekmann, M., Blond, N., Colette, A., Coll, I., Curci, G., Foret, G., Hodzic, A., Mailler, S., Meleux, F., Monge, J.-L., Pison, I., Siour, G., Turquety, S., Valari, M., Vautard, R., and Vivanco, M. G.: CHIMERE 2013: a model for regional atmospheric composition modelling, Geosci. Model Dev., 6, 981–1028, https://doi.org/10.5194/gmd-6-981-2013, 2013.

Mikhailov, E. F., Mironova, S., Mironov, G., Vlasenko, S., Panov, A., Chi, X., Walter, D., Carbone, S., Artaxo, P., Heimann, M., Lavric, J., Pöschl, U., and Andreae, M. O.: Long-term measurements (2010–2014) of carbonaceous aerosol and carbon monoxide at the Zotino Tall Tower Observatory (ZOTTO) in central Siberia, Atmos. Chem. Phys., 17, 14365-14392, https://doi: 10.5194/acp-17-14365-2017, 2017.

Mok, J., Krotkov, N. A., Arola, A., Torres, O., Jethva, H., Andrade, M., Labow, G., Eck, T. F., Li, Z., Dickerson, R. R., Stenchikov, G. L., Osipov, S., and Ren, X.: Impacts of brown carbon from biomass burning on surface UV and ozone photochemistry in the Amazon Basin, Sci. Rep.-UK, 6, 36940, https://doi.org/10.1038/srep36940, 2016.

Morgan, W. T., Allan, J. D., Bauguitte, S., Darbyshire, E., Flynn, M. J., Lee, J., Liu, D., Johnson, B., Haywood, J., Longo, K. M., Artaxo, P. E., and Coe, H.: Transformation and ageing of biomass burning carbonaceous aerosol over tropical South America from aircraft in situ measurements during SAMBBA, Atmos. Chem. Phys., 20, 5309–5326, https://doi.org/10.5194/acp-20-5309-2020, 2020.

NCEP: NCEP FNL Operational Model Global Tropospheric Analyses, continuing from July 1999, available at: https://rda.ucar.edu/datasets/ds083.2/ (last access: 1 April 2020), https://doi.org/10.5065/D6M043C6, 2017.

Oris, F., Asselin, H., Ali, A., Finsinger, W., and Bergeron, Y.: Effect of increased fire activity on global warming in the boreal forest, Environ. Rev., 22, 206-219, https://doi.org/10.1139/er-2013-0062, 2014.

Park, R. J., Kim, M. J., Jeong, J. I., Youn, D., and Kim, S.: A contribution of brown carbon aerosol to the aerosol light absorption and its radiative forcing in East Asia, Atmos. Environ., 44, 1414-1421, 2010.

Péré, J. C., Bessagnet, B., Mallet, M., Waquet, F., Chiapello, I., Minvielle, F., Pont, V., and Menut, L.: Direct radiative effect of the Russian wildfires and its impact on air temperature and atmospheric dynamics during August 2010, Atmos. Chem. Phys., 14, 1999–2013, https://doi.org/10.5194/acp-14-1999-2014, 2014.

Petrenko, M., Kahn, R., Chin, M., Soja, A., Kucsera, T., and Harshvardhan: The use of satellite-measured aerosol optical depth to constrain biomass burning emissions source strength in the global model GOCART, J. Geophys. Res., 117, D18212, doi:10.1029/2012JD017870, 2012.

Petters, M. D., and Kreidenweis, S. M.: A single parameter representation of hygroscopic growth and cloud condensation nucleus activity, Atmos. Chem. Phys., 7, 1961–1971, https://doi.org/10.5194/acp-7-1961-2007, 2007.

Petters, M. D., Carrico, C. M., Kreidenweis, S. M., Prenni, A. J., DeMott, P. J., Collett, J. L., and Moosmuller, H.: Cloud condensation nucleation activity of biomass burning aerosol, J. Geophys. Res., 114, D22205, https://doi.org/10.1029/2009JD012353, 2009.

Pokhrel, R. P., Beamesderfer, E. R., Wagner, N. L., Langridge, J. M., Lack, D. A., Jayarathne, T., Stone, E. A., Stockwell, C. E., Yokelson, R. J., and Murphy, S. M.: Relative importance of black carbon, brown carbon, and absorption enhancement from clear coatings in biomass burning emissions, Atmos. Chem. Phys., 17, 5063–5078, https://doi.org/10.5194/acp-17-5063-2017, 2017.

Press, W. H., Teukolsky, S. A., Vetterling, W. T., and Flannery, B. P.: Numerical Recipes, 2nd edition, Cambridge University Press, 1992.

Reddington, C. L., Spracklen, D. V., Artaxo, P., Ridley, D. A., Rizzo, L. V., and Arana, A.: Analysis of particulate emissions from tropical biomass burning using a global aerosol model and long-term surface observations, Atmos. Chem. Phys., 16, 11083–11106, https://doi.org/10.5194/acp-16-11083-2016, 2016.

Reid, J. S., Koppmann, R., Eck, T. F., and Eleuterio, D. P.: A review of biomass burning emissions part II: intensive physical properties of biomass burning particles, Atmos. Chem. Phys., 5, 799–825, https://doi.org/10.5194/acp-5-799-2005, 2005a.

Reid, J. S., Eck, T. F., Christopher, S. A., Koppmann, R., Dubovik, O., Eleuterio, D. P., Holben, B. N., Reid, E. A., and Zhang, J.: A review of biomass burning emissions part III: intensive optical properties of biomass burning particles, Atmos. Chem. Phys., 5, 827–849, https://doi.org/10.5194/acp-5-827-2005, 2005b.

Robinson, A. L., Donahue, N. M., Shrivastava, M. K., Weitkamp, E. A., Sage, A. M., Grieshop, A. P., Lane, T. E., Pierce, J. R., and Pandis, S. N.: Rethinking organic aerosols: Semivolatile emissions and photochemical aging, Science, 315, 1259–1262, https://doi.org/10.1126/science.1133061, 2007.

Sakamoto, K. M., Allan, J. D. Coe, H., Taylor, J. W., Duck, T. J., and Pierce, J. R.: Aged boreal biomass-burning aerosol size distributions from BORTAS 2011, Atmos. Chem. Phys., 15, 1633-1646, https://doi.org/10.5194/acp-15-1633-2015, 2015.

Saleh, R., Hennigan, C. J., McMeeking, G. R., Chuang, W. K., Robinson, E. S., Coe, H., Donahue, N. M., and Robinson, A. L.: Absorptivity of brown carbon in fresh and photo-chemically aged biomass-burning emissions, Atmos. Chem. Phys., 13, 7683–7693, https://doi.org/10.5194/acp-13-7683-2013, 2013.

Saleh, R., Robinson, E. S., Tkacik, D. S., Ahern, A. T., Liu, S., Aiken, A. C., Sullivan, R. C., Presto, A. A., Dubey, M. K., Yokelson, R. J., Donahue, N. M., and Robinson, A. L.: Brownness of organics in aerosols from biomass burning linked to their black carbon content, Nat. Geosci., 7, 647–650, https://doi.org/10.1038/ngeo2220, 2014.

Saleh, R., Marks, M., Heo, J., Adams, P. J., Donahue, N. M., and Robinson, A. L.: Contribution of brown carbon and lensing to the direct radiative effect of carbonaceous aerosols from biomass and biofuel burning emissions, J. Geophys. Res.-Atmos., 120, 10285–10296, 2015.

Salomonson, V. V., Barnes, W. L., Maymon, P. W., Montgomery, H. E., and Ostrow, H.: MODIS: advanced facility instrument for studies of the Earth as a system, IEEE T. Geosci. Remote, 27, 145–153, 1989.

Samset, B. H., Stjern, C. W., Andrews, E., Kahn, R. A., Myhre, G., Schulz, M., and Schuster, G. L.: Aerosol absorption: progress towards global and regional constraints, Curr. Clim. Change Rep., 4 (2), 65–83, https://doi.org/10.1007/s40641-018-0091-42018, 2018.

Sand, M., Berntsen, T., von Salzen, K., Flanner, M., Langner, J., and Victor, D.: Response of Arctic temperature to changes in emissions of short-lived climate forcers, Nat. Clim. Change, 6, 286–289, https://doi.org/10.1038/nclimate2880, 2015.

Selimovic, V., Yokelson, R. J., McMeeking, G. R., and Coefield, S.: In situ measurements of trace gases, PM, and aerosol optical properties during the 2017 NW US wildfire smoke event, Atmos. Chem. Phys., 19, 3905–3926, https://doi.org/10.5194/acp-19-3905-2019, 2019.

Shi, S., Cheng, T., Gu X., Guo, H., Wu, Y., and Wang, Y.: Biomass burning aerosol characteristics for different vegetation types in different aging periods, Environ. Int., 126, 504-511, https://doi.org/10.1016/j.envint.2019.02.073, 2019.

Shiraiwa, M., Li, Y., Tsimpidi, A. P., Karydis, V. A., Berkemeier, T., Pandis, S. N., Lelieveld, J., Koop, T., and Pöoschl, U.: Global distribution of particle phase state in atmospheric secondary organic aerosols, Nat. Commun., 8, 15002, https://doi.org/10.1038/ncomms15002, 2017.

Shrivastava, M., Easter, R., Liu, X., Zelenyuk, A., Singh, B., Zhang, K., Ma, P-L, Chand, D., Ghan, S., Jimenez, J. L., Zhang, Q., Fast, J., Rasch, P., and Tiitta, P.: Global transformation and fate of SOA: Implications of low volatility SOA and gas phase fragmentation reactions, J. Geophys. Res.-Atmos., 120, 4169–4195, https://doi.org/10.1002/2014JD022563, 2015.

Shrivastava, M., Cappa, C., Fan, J., Goldstein, A., Guenther, A., Jimenez, J., Kuang, C., Laskin, A., Martin, S., Ng, N., Petaja, T., Pierce, J., Rasch, P., Roldin, P., Seinfeld, J., Shilling, J., Smith, J., Thornton, J., Volkamer, R., Wang, J., Worsnop, D., Zaveri, R., Zelenyuk, A., and Zhang, Q.: Recent advances in understanding secondary organic aerosol: Implications for global climate forcing, Rev. Geophys., 55, 509–559, https://doi.org/10.1002/2016RG000540, 2017.

Sitnov, S.A., Mokhov, I.I., Gorchakov, G.I., Dzhola, A. V.: Smoke haze over the European part of Russia in the summer of 2016: A link to wildfires in Siberia and atmospheric circulation anomalies, Russ. Meteorol. Hydrol., 42, 518, https://doi.org/10.3103/S1068373917080052, 2017.

Sitnov, S.A., Mokhov, I.I., and Likhosherstova, A.A.: Exploring large-scale black-carbon air pollution over Northern Eurasia in summer 2016 using MERRA-2 reanalysis data, Atmos. Res., 235, 104763, DOI: 10.1016/j.atmosres.2019.104763, 2020.

Skamarock, W. C., Klemp, J. B., Dudhia, J., Gill, D. O., Barker, D. M., Duda, M. G., Huang, X.-Y., Wang, W., and Powers, J. G.: A Description of the advanced research WRF version 3, NCAR Tech. Notes–475CSTR, Boulder, Colorado, USA, 113 pp., 2008.

Sofiev, M., Ermakova, T., and Vankevich, R.: Evaluation of the smoke-injection height from wild-land fires using remote-sensing data, Atmos. Chem. Phys., 12, 1995–2006, https://doi.org/10.5194/acp-12-1995-2012, 2012.

Stromatas, S., Turquety, S., Menut, L., Chepfer, H., Péré, J. C., Cesana, G., and Bessagnet, B.: Lidar signal simulation for the evaluation of aerosols in chemistry transport models, Geosci. Model Dev., 5, 1543–1564, https://doi.org/10.5194/gmd-5-1543-2012, 2012.

Sumlin, B. J., Pandey, A., Walker, M. J., Pattison, R. S., Williams, B. J., and Chakrabarty, R. K., Atmospheric photooxidation diminishes light absorption by primary brown carbon aerosol from biomass burning: Environmental Science & Technology Letters, 4, 540-545, doi:10.1021/acs.estlett.7b00393, 2017.

Taylor, J. W., Wu, H., Szpek, K., Bower, K., Crawford, I., Flynn, M. J., Williams, P. I., Dorsey, J., Langridge, J. M., Cotterell, M. I., Fox, C., Davies, N. W., Haywood, J. M., and Coe, H.: Absorption closure in highly aged biomass burning smoke, Atmos. Chem. Phys. Discuss., https://doi.org/10.5194/acp-2020-333, in review, 2020.

Thornberry, T., Froyd, K. D., Murphy, D. M., Thomson, D. S., Anderson, B. E., Thornhill, K. L., and Winstead, E. L.: Persistence of organic carbon in heated aerosol residuals measured during Tropical Composition Cloud and Climate Coupling (TC4), J. Geophys. Res., 115, D00J02, https://doi.org/10.1029/2009jd012721, 2010.

Tiitta, P., Leskinen, A., Hao, L., Yli-Pirilä, P., Kortelainen, M., Grigonyte, J., Tissari, J., Lamberg, H., Hartikainen, A., Kuuspalo, K., Kortelainen, A.-M., Virtanen, A., Lehtinen, K. E. J., Komppula, M., Pieber, S., Prévôt, A. S. H., Onasch, T. B., Worsnop, D. R., Czech, H., Zimmermann, R., Jokiniemi, J., and Sippula, O.: Transformation of logwood combustion emissions in a smog chamber: formation of secondary organic aerosol and changes in the primary organic aerosol upon daytime and nighttime aging, Atmos. Chem. Phys., 16, 13251-13269, https://doi.org/10.5194/acp-16-13251-2016, 2016.

Tsimpidi, A. P., Karydis, V. A., Pozzer, A., Pandis, S. N., and Lelieveld, J.: ORACLE 2-D (v2.0): an efficient module to compute the volatility and oxygen content of organic aerosol with a global chemistry-climate model, Geosci. Model Dev., 11, 3369-3389, https://doi.org/10.5194/gmd-11-3369-2018, 2018.

Toon, O. and Ackerman, T.: Algorithms for the calculation of scattering by stratified spheres, Appl. Optics, 20, 3657–3660, 1981.

Torres, O. O.: OMI/Aura Near UV Aerosol Optical Depth and Single Scattering Albedo 1-orbit L2 Swath 1324 km V003, Greenbelt, MD, USA, Goddard Earth Sciences Data and Information Services Center (GES DISC), https://doi.org/10.5067/Aura/OMI/DATA2004 (last access: 19 April 2020), 2006.

Torres, O., Tanskanen, A., Veihelmann, B., Ahn, C., Braak, R., Bhartia, P. K., Veefkind, P., and Levelt, P.: Aerosols and surface UV products from Ozone Monitoring Instrument observations: An overview, J. Geophys. Res., 112, D24S47, https://doi.org/10.1029/2007JD008809, 2007.

Torres, O., Ahn, C., and Chen, Z.: Improvements to the OMI near-UV aerosol algorithm using A-train CALIOP and AIRS observations, Atmos. Meas. Tech., 6, 3257–3270, https://doi.org/10.5194/amt-6-3257-2013, 2013.

Tosca, M. G., Randerson, J. T., and Zender, C. S.: Global impact of smoke aerosols from landscape fires on climate and the Hadley circulation, Atmos. Chem. Phys., 13, 5227–5241, https://doi.org/10.5194/acp-13-5227-2013, 2013.

Tsigaridis, K., Daskalakis, N., Kanakidou, M., Adams, P. J., Artaxo, P., Bahadur, R., Balkanski, Y., Bauer, S. E., Bellouin, N., Benedetti, A., Bergman, T., Berntsen, T. K., Beukes, J. P., Bian, H., Carslaw, K. S., Chin, M., Curci, G., Diehl, T., Easter, R. C., Ghan, S. J., Gong, S. L., Hodzic, A., Hoyle, C. R., Iversen, T., Jathar, S., Jimenez, J. L., Kaiser, J. W., Kirkevag, A., Koch, D., Kokkola, H., Lee, Y. H., Lin, G., Liu, X., Luo, G., Ma, X., Mann, W., Mihalopoulos, N., Morcrette, J. J., Mueller, J. F., Myhre, G., Myriokefalitakis, S., Ng, N. L., O'Donnell, D., Penner, J. E., Pozzoli, L., Pringle, K. J., Russell, L. M., Schulz, M., Sciare, J., Seland, O., Shindell, D. T., Sillman, S., Skeie, R. B., Spracklen, D., Stavrakou, T., Steenrod, S. D., Takemura, T., Tiitta, P., Tilmes, S., Tost, H., van Noije, T., van Zyl, P. G., von Salzen, K., Yu, F., Wang, Z., Wang, Z., Zaveri, R. A., Zhang, H., Zhang, K., Zhang, Q., and Zhang, X.: The AeroCom evaluation and intercomparison of organic aerosol in global models, Atmos. Chem. Phys., 14, 10845–10895, https://doi.org/10.5194/acp-14-10845- 2014, 2014.

Tsigaridis, K. and Kanakidou, M.: The Present and Future of Secondary Organic Aerosol Direct Forcing on Climate, Current Climate Change Reports, 4, 1–15, https://doi.org/10.1007/s40641-018-0092-3, 2018.

Vakkari, V., Beukes, J. P., Dal Maso, M., Aurela, M., Josipovic, M., and van Zyl, P. G.: Major secondary aerosol formation in southern African open biomass burning plumes, Nature Geosci., 11, 580–583, https://doi.org/10.1038/s41561-018-0170-0, 2018.

Wang, R., Balkanski, Y., Boucher, O., Ciais, P., Schuster, G. L., Chevallier, F., Samset, B. H., Liu, J., Piao, S., Valari, M., and Tao, S., Estimation of global black carbon direct radiative forcing and its uncertainty constrained by observations: J. Geophys. Res., 121, 5948-5971, doi:10.1002/2015JD024326, 2016.

Wang, X., Heald, C. L., Sedlacek, A. J., de Sá, S. S., Martin, S. T., Alexander, M. L., Watson, T. B., Aiken, A. C., Springston, S. R., and Artaxo, P.: Deriving brown carbon from multiwavelength absorption measurements: method and application to AERONET and Aethalometer observations, Atmos. Chem. Phys., 16, 12733–12752, https://doi.org/10.5194/acp-16-12733-2016, 2016.

Wang, X., Heald, C. L., Liu, J., Weber, R. J., Campuzano-Jost, P., Jimenez, J. L., Schwarz, J. P., and Perring, A. E.: Exploring the observational constraints on the simulation of brown carbon, Atmos. Chem. Phys., 18, 635–653, https://doi.org/10.5194/acp-18-635-2018, 2018.

Warneke, C., Bahreini, R., Brioude, J., Brock, C. A., de Gouw, J. A., Fahey, D. W., Froyd, K. D., Holloway, J. S., Middlebrook, A., Miller, L., Montzka, S., Murphy, D. M., Peischl, J., Ryerson, T. B., Schwarz, J. P., Spackman, J. R., and Veres, P.: Biomass burning in Siberia and Kazakhstan as an important source for haze over the Alaskan Arctic in April 2008, Geophysical Research Letters, 36, https://doi.org/10.1029/2008GL036194, 2009.

Wong, J. P. S., Nenes, A., and Weber, R. J.: Changes in light absorptivity of molecular weight separated brown carbon due to photolytic aging, Environ. Sci. Technol., 51, 8414–8421, https://doi.org/10.1021/acs.est.7b01739, 2017.

Wong, J. P. S., Tsagkaraki, M., Tsiodra, I., Mihalopoulos, N., Violaki, K., Kanakidou, M., Sciare, J., Nenes, A., and Weber, R. J.: Atmospheric evolution of molecular-weight-separated brown carbon from biomass burning, Atmos. Chem. Phys., 19, 7319–7334, https://doi.org/10.5194/acp-19-7319-2019, 2019.

Wu, C., Wu, D., and Yu, J. Z.: Quantifying black carbon light absorption enhancement with a novel statistical approach, Atmos. Chem. Phys., 18, 289–309, https://doi.org/10.5194/acp-18-289-2018, 2018.

Yasunari, T., Kim, K.-M., Da Silva, A., Hayasaki, M., Akiyama, M., Murao, N., Extreme air pollution events in Hokkaido, Japan, traced back to early snowmelt and large-scale wildfires over East Eurasia: Case studies, Scientific Reports, 8, 6413, https://doi.org /10.1038/s41598-018-24335-w, 2018.

Yokelson, R. J., Crounse, J. D., DeCarlo, P. F., Karl, T., Urbanski, S., Atlas, E., Campos, T., Shinozuka, Y., Kapustin, V., Clarke, A. D., Weinheimer, A., Knapp, D. J., Montzka, D. D., Holloway, J., Weibring, P., Flocke, F., Zheng, W., Toohey, D., Wennberg, P. O., Wiedinmyer, C., Mauldin, L., Fried, A., Richter, D., Walega, J., Jimenez, J. L., Adachi, K., Buseck, P. R., Hall, S. R., and Shetter, R.: Emissions from biomass burning in the Yucatan, Atmos. Chem. Phys., 9, 5785–5812, https://doi.org/10.5194/acp-9-5785-2009, 2009.

Zhang, A., Wang, Y., Zhang, Y., Weber, R. J., Song, Y., Ke, Z., and Zou, Y.: Modeling the global radiative effect of brown carbon: a potentially larger heating source in the tropical free troposphere than black carbon, Atmos. Chem. Phys., 20, 1901–1920, https://doi.org/10.5194/acp-20-1901-2020, 2020.

Zhang, L., Gong, S., Padro, J., and Barrie, L.: A size-segregated particle dry deposition scheme for an atmospheric aerosol module, Atmos. Environ., 35, 549–560, 2001.

Zhang, L., Henze, D. K., Grell, G. A., Carmichael, G. R., Bousserez, N., Zhang, Q., Torres, O., Ahn, C., Lu, Z., Cao, J., and Mao, Y.: Constraining black carbon aerosol over Asia using OMI aerosol absorption optical depth and the adjoint of GEOS-Chem, Atmos. Chem. Phys., 15, 10281–10308, https://doi.org/10.5194/acp-15- 10281-2015, 2015.

Zhang, Y., Huang, J.-P., Henze, D. K., and Seinfeld, J. H.: Role of isoprene in secondary organic aerosol formation on a regional scale, J. Geophys. Res. Atmos., 112, D20207, https://doi.org/10.1029/2007JD008675, 2007.

Zhong, M. and Jang, M.: Dynamic light absorption of biomass-burning organic carbon photochemically aged under natural sunlight, Atmos. Chem. Phys., 14, 1517–1525, https://doi.org/10.5194/acp-14-1517-2014, 2014.

Zhou, S., Collier, S., Jaffe, D. A., Briggs, N. L., Hee, J., Sedlacek III, A. J., Kleinman, L., Onasch, T. B., and Zhang, Q.: Regional influence of wildfires on aerosol chemistry in the western US and insights into atmospheric aging of biomass burning organic aerosol, Atmos. Chem. Phys., 17, 2477–2493, https://doi.org/10.5194/acp-17-2477-2017, 2017.

https://doi.org/10.5194/acp-2020-591
Preprint. Discussion started: 29 June 2020

Table 1. Parameters of the species representing the evolution of BB OA in the framework of the simplified VBS scheme

Species name	Volatility, C* (μg m^{-3})	Molar mass	Enthalpy of evaporation, ΔH_{vap} (kJ mol^{-1})
LV-POA	10^0	216	85
MV-POA	10^2	216	77
LV-SOA	10^0	144	85
MV-SOA	10^2	135	77
HV-SOA	10^3	131	73
NTVOCs	∞	113	-

5

Table 2. Reactions representing the evolution of BB OA in the simplified VBS scheme and their OH reaction rates (k_{OH})

	Reaction	k_{OH} (cm^3 molec^{-1} s^{-1})
(R1)	MV-POA + OH → 1.3 LV-SOA + OH	4×10^{-11}
(R2)	LV-POA + OH → 1.3 LV-SOA + OH	4×10^{-11}
(R3)	NTVOC + OH → ξ_1[(a)] 0.33 HV-SOA + (1-ξ_1) 0.30 LV-SOA + OH	4×10^{-11}
(R4)	HV-SOA + OH → MV-SOA + OH	4×10^{-11}
(R5)	MV-SOA+ OH → ξ_2[(a)] LV-SOA + OH	1×10^{-11}
(R6)	LV-SOA+ OH → ξ_2 LV-SOA + OH	1×10^{-11}

[(a)] ξ_1 and ξ_2 are adjustable parameters, which have been evaluated as: ξ_1=0.85, ξ_2=0.15

10

https://doi.org/10.5194/acp-2020-591
Preprint. Discussion started: 29 June 2020

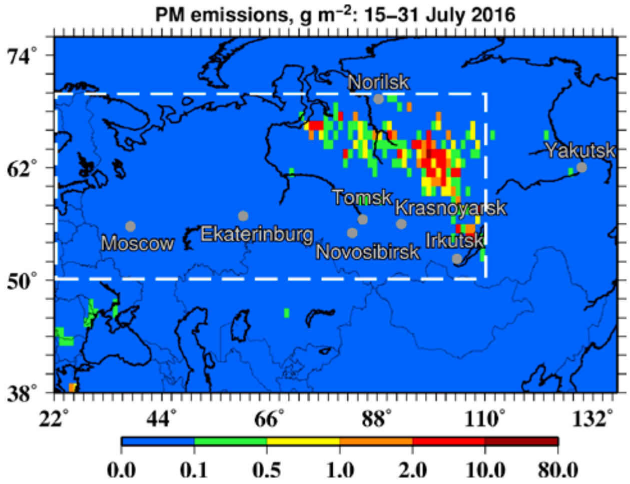

Figure 1. Spatial distribution of the total emissions (g m^{-2}) of particulate matter from fires in the period from 15 to 31 July 2016. The emissions were computed using the MODIS FRP data (see Sect. 2.3) and are shown over the CHIMERE domain specified in this study. A dashed white rectangle indicates the study region.

https://doi.org/10.5194/acp-2020-591
Preprint. Discussion started: 29 June 2020

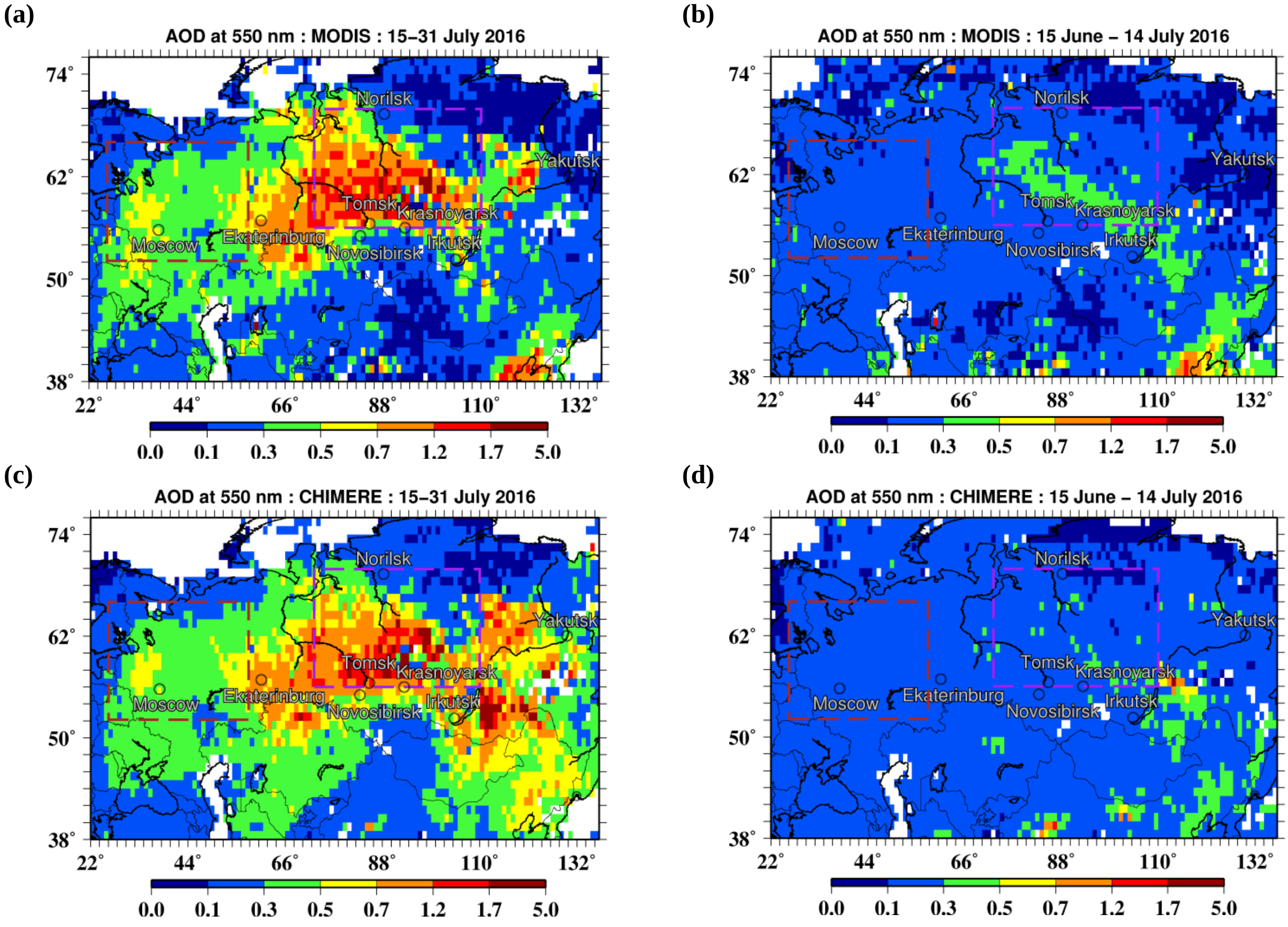

Figure 2. Spatial distributions of the temporal averages of AOD (at 550 nm) in the periods (a,c) from 15 to 31 July 2016 and (b,d) from 15 June to 14 July 2016 according to (a,b) the MODIS observations and (c,d) the combined CHIMERE simulations for the ‘bb_vbs’ and ‘bgr’ scenarios. The distributions represent the ancillary sets of AOD data that were selected irrespective of the availability of the corresponding AAOD retrievals. The rectangles depict the “source” (purple lines) and “receptor” (dark red lines) regions covering parts of Siberia and (mostly) the European territory of Russia, respectively.

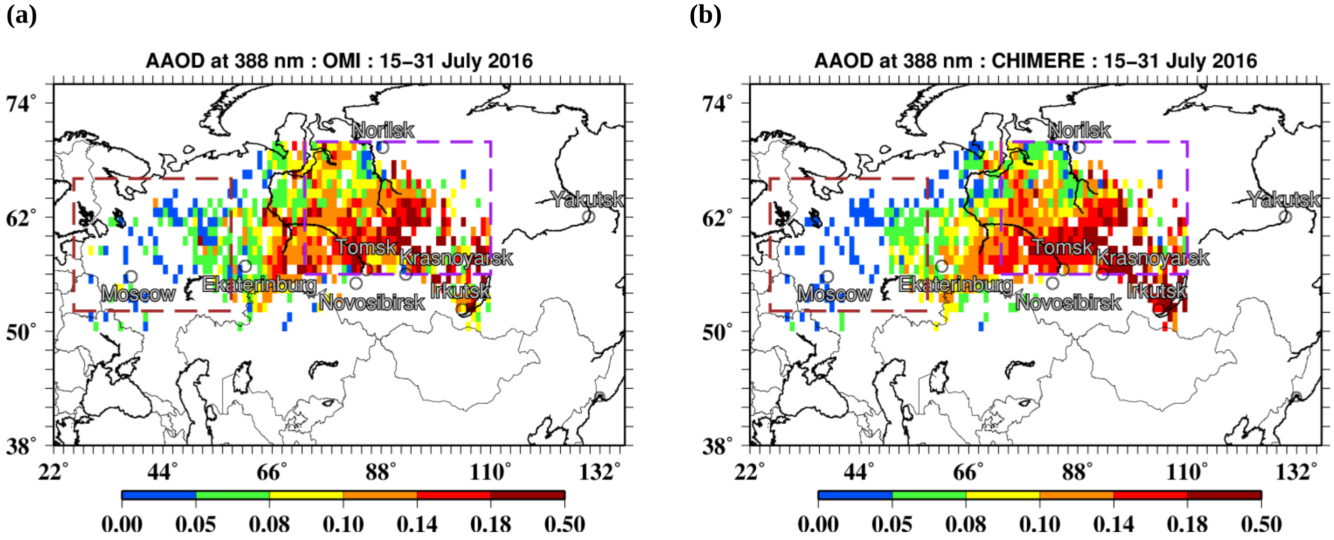

Figure 3. Spatial distributions of temporal averages of AAOD (at 388 nm) in the period from 15 to 31 July 2016 according to (a) the OMI observations and (b) CHIMERE simulations for the 'bb_vbs' scenario. The AAOD data represent only BB aerosol in the study region according to the selection criterion specified in the OMAERUV data product. The rectangles depict the source and receptor regions as in Fig. 2.

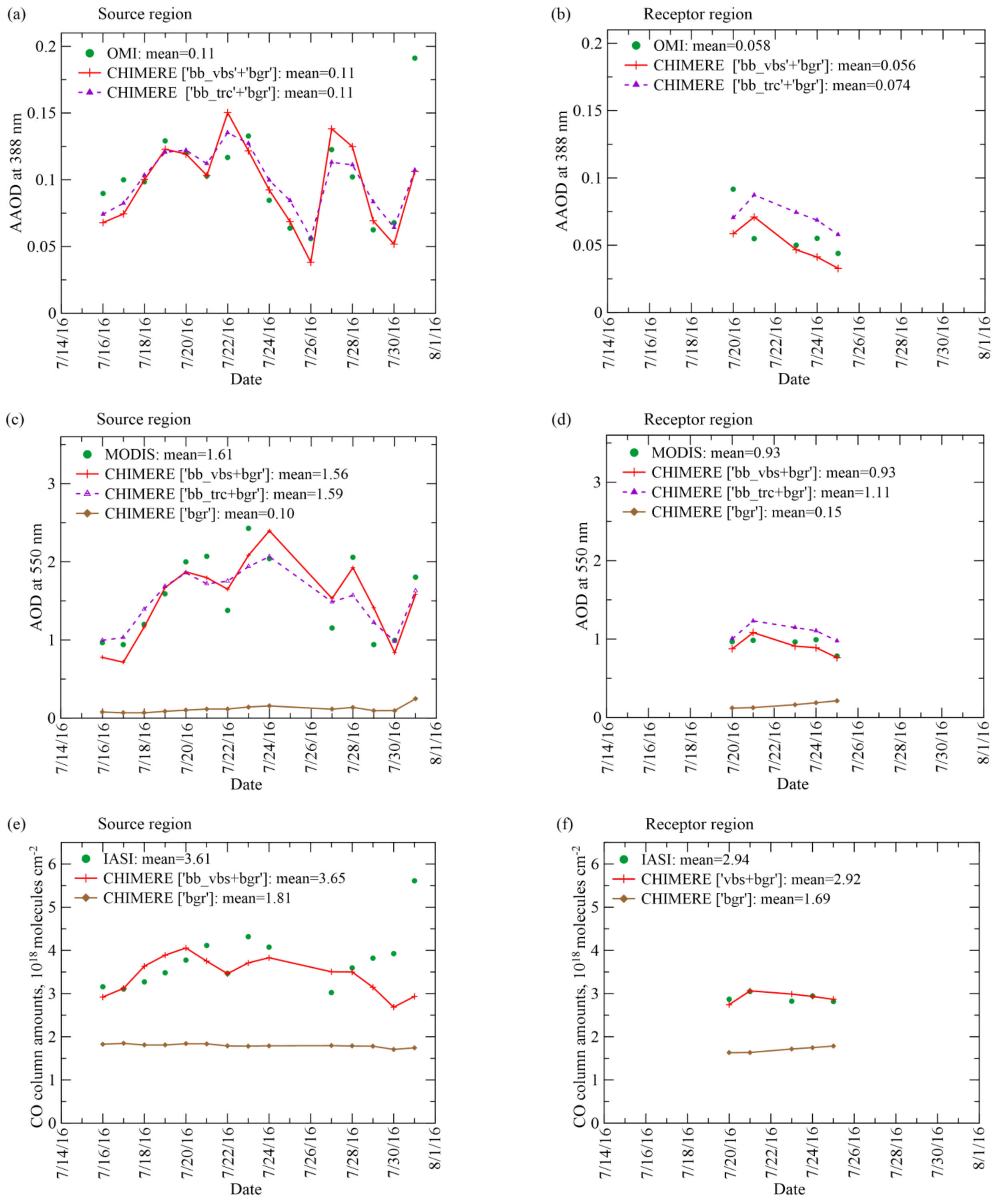

Figure 4. Time series of the daily (a,b) AAOD, (c,d) AOD, and (e,f) CO values averaged over the study region according to the satellite

observations and the CHIMERE simulations under the different model scenarios for the (a,c,e) “source” and (b,d,f) “receptor” regions indicated in Fig. 2. All the data were selected consistently. Note that the simulations for the ‘bgr’ (background) scenario are shown after applying the de-biasing procedure (see Sect. 2.5). The background AAOD is not evaluated in this study and therefore not shown. Taking into account that the time series are very short, the correlation coefficient has not been evaluated (as its values are not sufficiently robust).

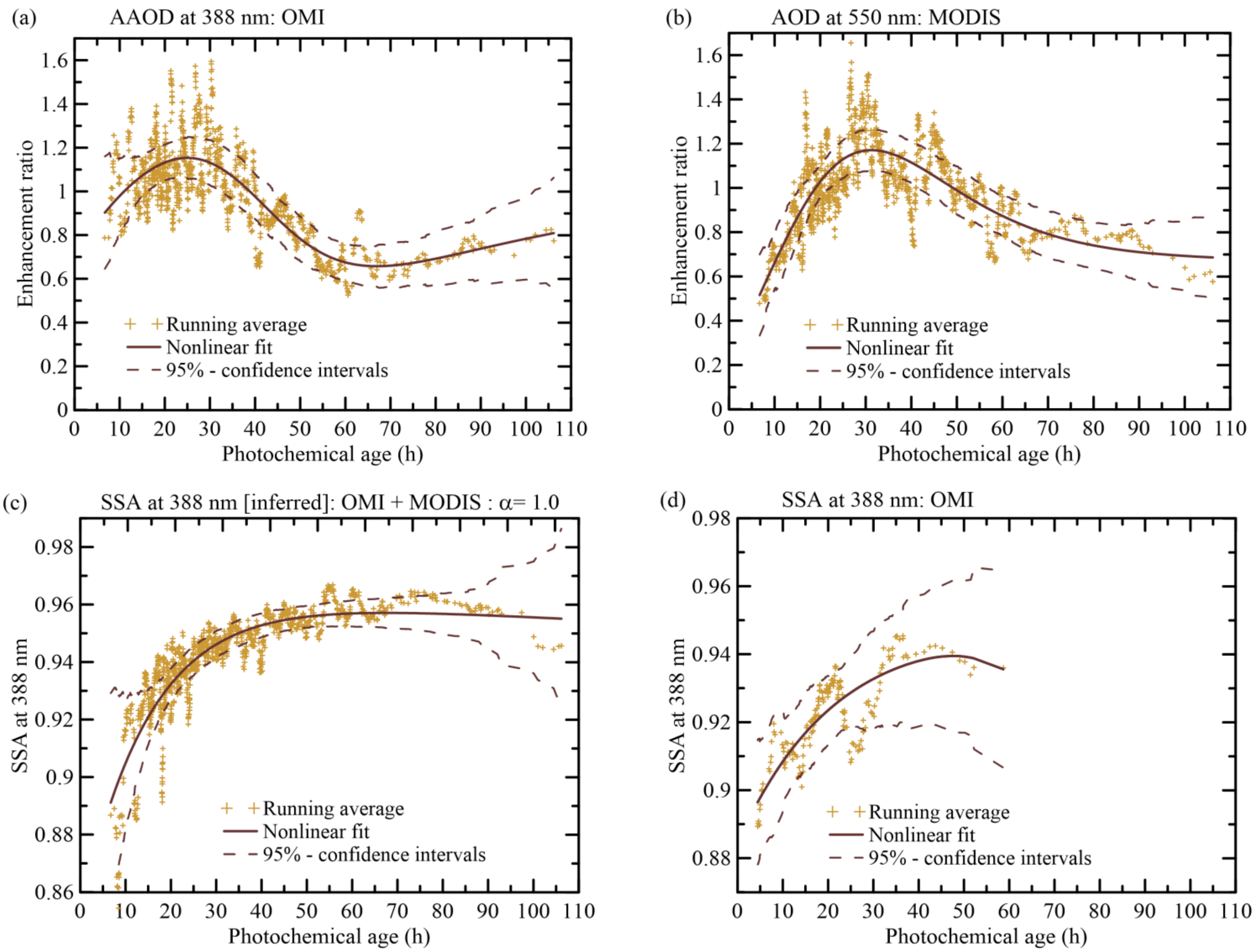

Figure 5. Nonlinear approximations (see Eq. 5) of the dependencies of (a, b) EnRs for AAOD (388 nm) and AOD (550 nm) and (c, d) SSA (388 nm) on the photochemical age of BB aerosol. Also shown are the running averages over each consecutive 15 data points (for EnRs or SSA) arranged with respect to the photochemical age as well as the 95 % confidence intervals for the approximations. The SSA values approximated in panel (c) are inferred from the OMI AAOD and MODIS AOD observations, while those presented in panel (d) are provided directly in the OMAERUV data product.

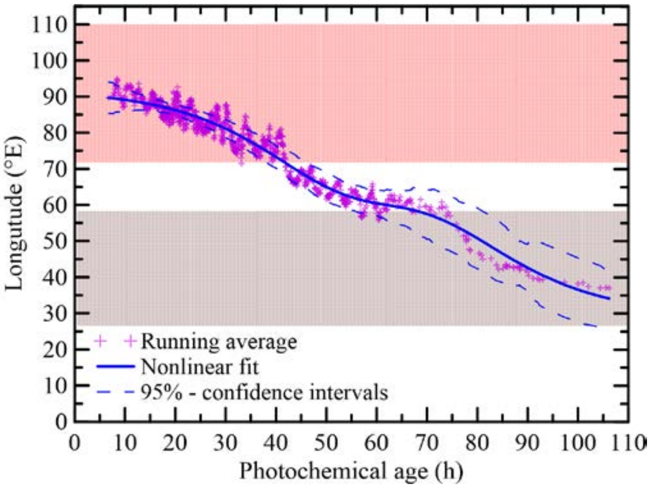

Figure 6. Dependence of the longitude of the instant location of a given BB plume on its photochemical age. The shaded areas indicate the ranges of longitudes of the source (red shade) and receptor (brown shade) regions shown in Fig. 2.

5

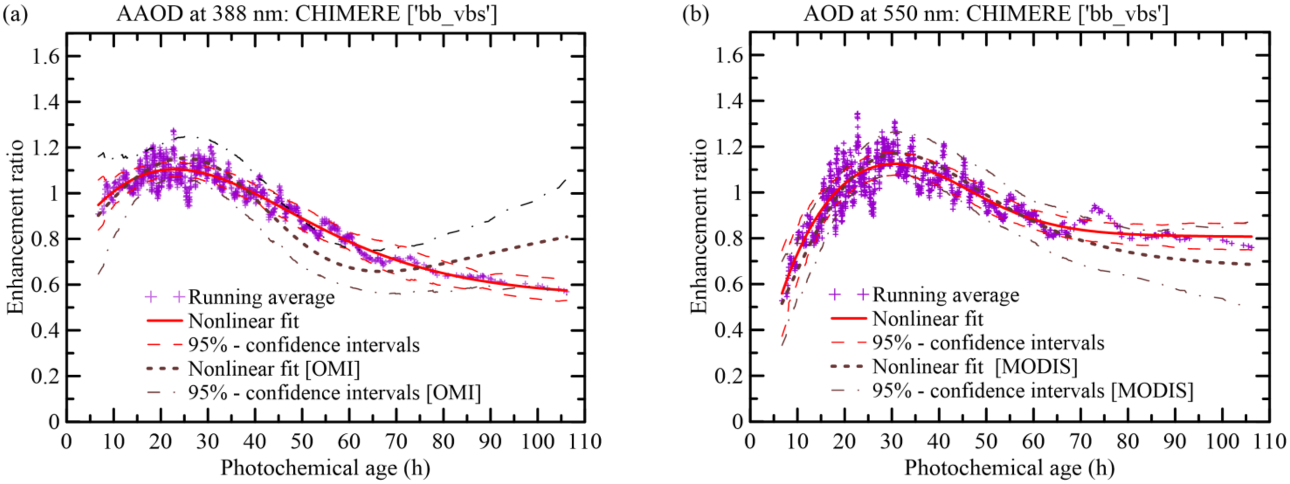

Figure 7. The same as in Figs. 6a, b but obtained using the CHIMERE simulations for the ‘bb_vbs’ scenario. The dependencies from Figs. 6a, b, and their confidence intervals are also shown for comparison.

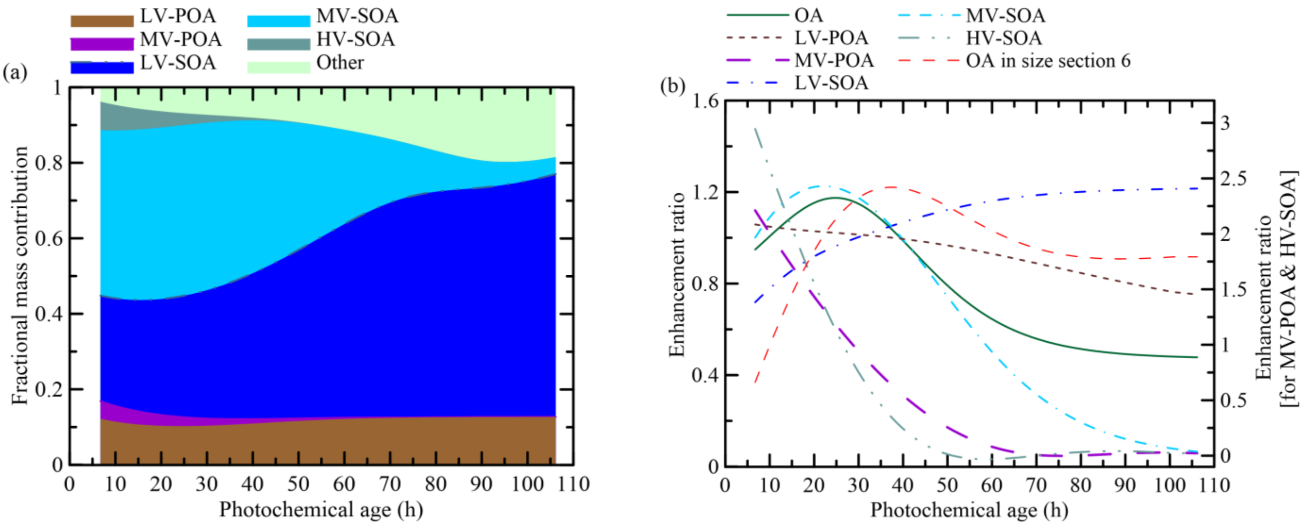

Figure 8. Evolution of the key model species determining the composition of BB aerosol in the CHIMERE simulation for the 'bb_vbs' scenario: (a) fractional contributions of the model species in the mass columnar concentration of BB aerosol, (b) the normalized EnRs of columnar concentrations of organic species in the particulate phase in the simulations for the 'bb_vbs' scenario with respect to OA concentration in the simulations for the 'bb_trc' scenario, along with similar enhancement ratios for the total columnar OA concentration and OA concentration in the 6th bin (310-630 nm) of the particle size distribution in CHIMERE. Note that the EnRs for MV-POA and HV-SOA are presented using the right ordinate axis.

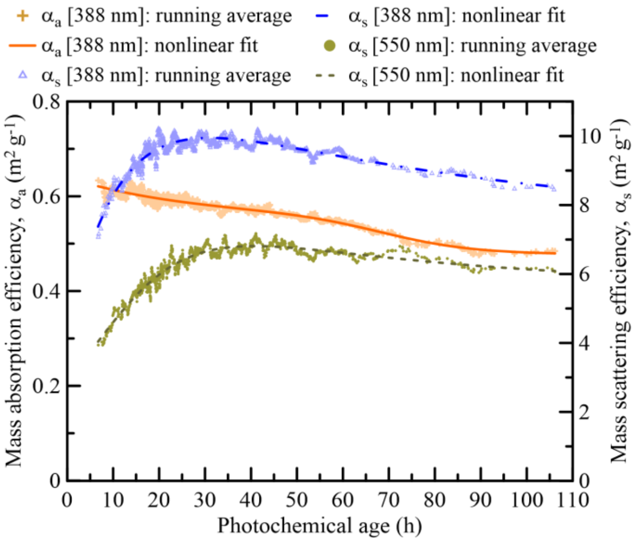

Figure 9. Evolution of the mass absorption efficiency at 388 nm (left axis) and mass scattering efficiency at 388 and 550 nm (right axis) according to the simulations with the CHIMERE CTM and OPTSIM module for the 'bb_vbs' scenario.

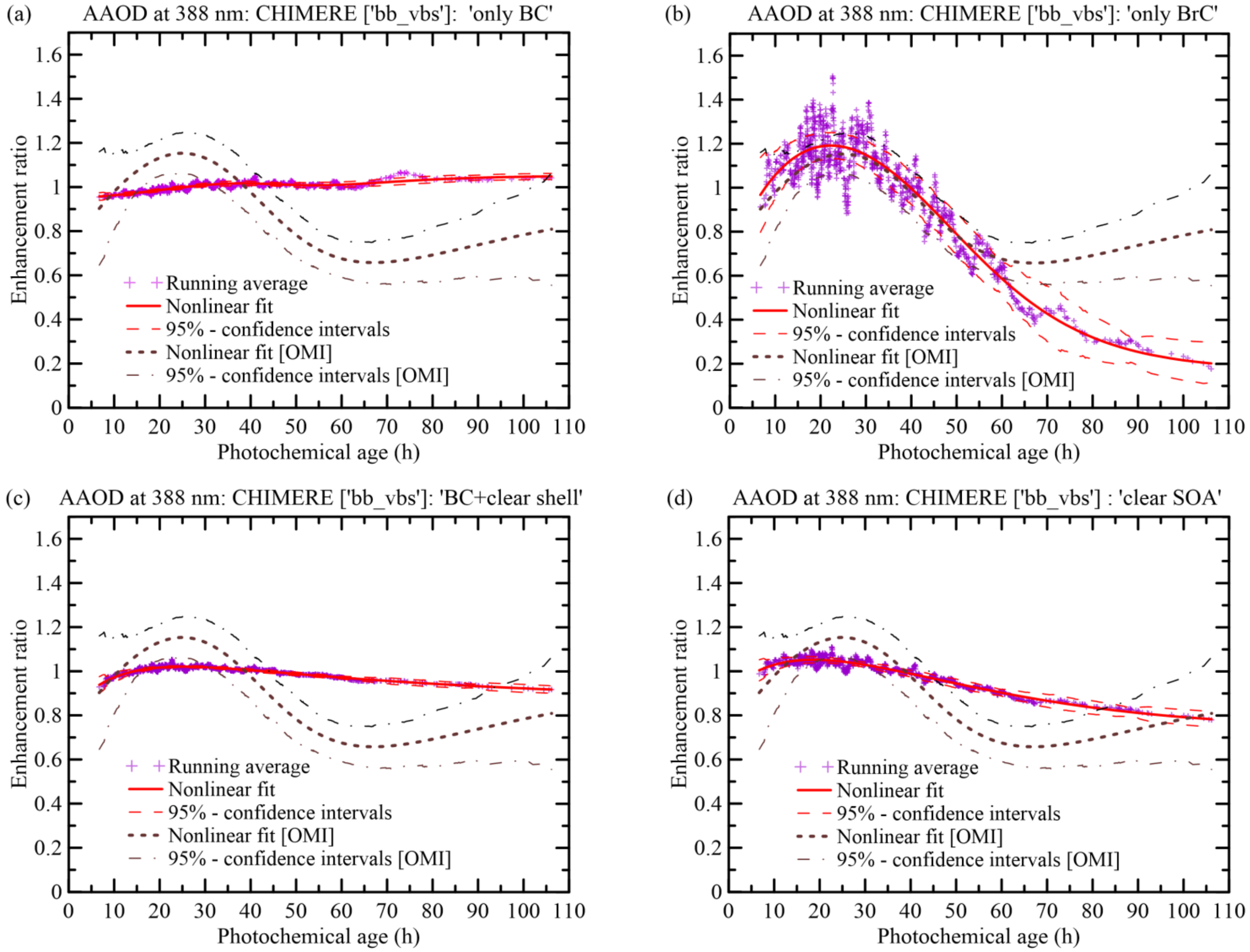

Figure 10. Evolution of EnR_{abs} according to model results for several limiting cases involving different specifications of the optical properties of the individual components of BB aerosol: (a) absorption is determined only by BC, (b) absorption is determined only by BrC, (c) absorption is determined only by BC core surrounded by a non-absorbing shell, (d) absorption is determined only by both BC core and OA shell, but SOA is non-absorbing. The trends in EnR_{abs} according to the analysis of satellite observations (Figs. 6a) and its confidence intervals are also shown for comparison.